

# Incorporating Prior Knowledge into Neural Networks through an Implicit Composite Kernel

Ziyang Jiang<sup>1</sup> Tongshu Zheng<sup>2</sup> Yiling Liu<sup>3</sup> David Carlson<sup>1</sup>

## Abstract

It is challenging to guide neural network (NN) learning with prior knowledge. In contrast, many known properties, such as spatial smoothness or seasonality, are straightforward to model by choosing an appropriate kernel in a Gaussian process (GP). Many deep learning applications could be enhanced by modeling such known properties. For example, convolutional neural networks (CNNs) are frequently used in remote sensing, which is subject to strong seasonal effects. We propose to blend the strengths of deep learning and the clear modeling capabilities of GPs by using a composite kernel that combines a kernel implicitly defined by a neural network with a second kernel function chosen to model known properties (e.g., seasonality). We implement this idea by combining a deep network and an efficient mapping based on the Nyström approximation, which we call Implicit Composite Kernel (ICK). We then adopt a sample-then-optimize approach to approximate the full GP posterior distribution. We demonstrate that ICK has superior performance and flexibility on both synthetic and real-world data sets. We believe that ICK framework can be used to include prior information into neural networks in many applications.

## 1. Introduction

In complex regression tasks, input data often contains *multiple sources of information*. These sources can be presented in both high-dimensional (e.g. images, audios, texts, etc.) and low-dimensional (e.g. timestamps, spatial locations, etc.) forms. A common approach to learn from high-dimensional information is to use neural networks (NNs) (Goodfellow et al., 2016; LeCun et al., 2015), as NNs are powerful enough to capture the relationship between complex high-dimensional data and target variables of interest. In many areas, NNs are standard practice, such as the dominance of Convolutional Neural Networks (CNNs) for image analysis (Jiang et al., 2022; Zheng et al., 2021; 2020). In contrast, for low-dimensional information, we usually have

some prior knowledge on how the information relates to the predictions. As a concrete example, consider a remote sensing problem where we predict ground measurements from satellite imagery with associated timestamps. *A priori*, we expect the ground measurements to vary periodically with respect to time between summer and winter due to seasonal effects. We would typically use a CNN to capture the complex relationship between the imagery and the ground measurements. In this case, we want to guide the learning of the CNN with our prior knowledge about the seasonality. This is challenging because knowledge represented in NNs pertains mainly to correlation between network units instead of quantifiable statements (Marcus, 2018).

Conversely, Gaussian processes (GPs) have been used historically to incorporate relevant prior beliefs by specifying the appropriate form of its kernel (or covariance) function (Bishop & Nasrabadi, 2006; Williams & Rasmussen, 2006). One approach to modeling multiple sources of information is to assign a relevant kernel function to each source of information respectively and combine them through addition or multiplication, resulting in a *composite kernel function* (Duvenaud, 2014). This formulation means that specifying a kernel to match prior beliefs on one source of information is straightforward. Such composite kernel learning techniques are extensively used in many application areas such as multimedia data (McFee et al., 2011), neuroimaging (Zhang et al., 2011), spatial data analysis, and environmental data analysis (Kim et al., 2005; Petelin et al., 2013). In view of the clear modeling capabilities of GP, it is desirable to examine how a NN could be imbued with the same modeling ease.

In recent years, researchers have come up with a variety of methods to incorporate prior knowledge into NNs. These efforts can be broken into many categories, such as those that add prior information through loss terms like physics-informed NNs (Lagaris et al., 1998; Moseley et al., 2020). Here, we focus on the major category of those methods that build integrated models of NNs and GPs with various structures (Van der Wilk et al., 2017; Wilson et al., 2016; 2011). Related to our proposed methodology, Pearce et al. (Pearce et al., 2020) exploited the fact that a Bayesian neural network (BNN) approximates a GP to construct additive and multiplicative kernels, but they were limited to specific

predefined kernels. Matsubara et al. (Matsubara et al., 2020) then resolved this limitation by constructing priors of BNN parameters based on the ridgelet transform and its dual, but they did not explicitly show how their approach works for data with multiple sources of information. To our knowledge, no existing approach allows a modeler to choose any appropriate kernel over multiple sources.

We address this limitation by presenting a simple yet novel Implicit Composite Kernel (ICK) framework, which processes high-dimensional information using a kernel implicitly defined by a neural network and low-dimensional information using a chosen kernel function. The low-dimensional kernels are mapped into the neural network framework to create a straightforward and simple-to-learn implementation. Our key results and contributions are:

- We analytically show our ICK framework, under reasonable assumptions, is approximately equivalent to sampling from a Gaussian process regression (GPR) model with a composite kernel *a priori*.
- We adopt a sample-then-optimize procedure to ICK to approximate the full posterior distribution of a GP with a composite kernel.
- We show that ICK yields better performance on prediction and forecasting tasks, even with limited data.
- We show that ICK can flexibly capture the patterns of the low-dimensional information without bespoke pre-processing procedures or complex NN structures.

Based on these contributions, we believe ICK is useful in learning from complex *hybrid* data with prior knowledge, especially in remote sensing and spatial statistics.

## 2. Related Work

**Equivalence between NNs and GPs** The equivalence between GPs and randomly initialized single-layer NNs with infinite width was first shown by Neal (Neal, 1996). With the development of modern deep learning, researchers further extended this relationship to deep networks (Lee et al., 2017; Matthews et al., 2018) and convolutional neural networks (CNNs) (Garriga-Alonso et al., 2018). This relationship is crucial for showing the resemblance between GPR and our ICK framework, which is discussed in Section 4.1.

**NNs with prior knowledge** As mentioned before, one approach to equip NNs with prior knowledge is to modify the loss function. For example, Lagaris et al. (Lagaris et al., 1998) solved differential equations (DEs) using NNs by setting the loss to be a function whose derivative satisfies the DE conditions. Another approach is to build integrated models of NNs and kernel-based models. For example, Wilson et al. (Wilson et al., 2011) implemented a regression network with GP priors over latent variables and made inference by approximating the posterior using Variational

Bayes or sampling from the posterior using Gibbs sampling scheme. Garnelo et al. (Garnelo et al., 2018) introduced a class of neural latent variable models called Neural Processes (NPs) which are capable of learning efficiently from the data and adapting rapidly to new observations. Our ICK framework fuses prior knowledge into NNs by modulating the learnt features using another set of features outputted from a kernel-based mapping, which can also be viewed as an integrated model of NNs and kernel machines.

**GP with composite kernels** Composite kernel GPs are widely used in both machine learning (Duvenaud, 2014; Williams & Rasmussen, 2006) and geostatistical modeling (Datta et al., 2016; Gelfand & Schliep, 2016). GPR in geostatistical modeling is also known as *kriging* (Journel & Huijbregts, 1976; Krige, 1951), which serves as a surrogate model to replace expensive function evaluations. The inputs for a composite GP are usually low-dimensional (e.g. spatial distance) as GPs do not scale well with the number of samples for high-dimensional inputs (Bouhlef & Martins, 2019; Bouhlef et al., 2016). To overcome this issue, Pearce et al. (Pearce et al., 2020) and Matsubara et al. (Matsubara et al., 2020) developed BNN analogues for composite GPs. Similar to these studies, our ICK framework can also be viewed as a simulation for composite GPs.

**Approximation methods for GP** For large data sets, approximation methods are needed as exact kernel learning and inference scales  $\mathcal{O}(N^3)$ . Nyström low-rank matrix approximation (Drineas et al., 2005; Williams & Seeger, 2000) and Random Fourier Features (Rahimi & Recht, 2007; 2008) are two commonly used methods. A common technique is to choose inducing points as pseudo-inputs to efficiently approximate the full kernel matrix (Snelson & Ghahramani, 2005; Hensman et al., 2013). Our work is inspired by these approximation techniques and we use them as *transformation functions* to map the kernel matrix into latent space representations in Section 4.2.

## 3. Background

Before elaborating on the ICK framework, we introduce our notation, briefly go over the concepts of composite GPs, and describe the relationship between GPs and NNs.

### 3.1. Problem Setup

To formalize the problem, we have a training data set which contains  $N$  data points  $\mathbf{X} = [\mathbf{x}_i]_{i=1}^N = [\mathbf{x}_1, \mathbf{x}_2, \dots, \mathbf{x}_N]^T$  and the corresponding labels of these data points are  $\mathbf{y} = [y_i]_{i=1}^N = [y_1, y_2, \dots, y_N]^T$  where  $y_i \in \mathbb{R}$ . Each data point  $\mathbf{x}_i = \{\mathbf{x}_i^{(1)}, \mathbf{x}_i^{(2)}, \dots, \mathbf{x}_i^{(M)}\}$  is composed of information from  $M$  different sources where the  $m^{th}$  source of information of the  $i^{th}$  data point is denoted as  $\mathbf{x}_i^{(m)} \in \mathbb{R}^{D_m}$ . Our goal is to learn a function  $\hat{y}_i = f(\mathbf{x}_i) :$

$\{\mathbb{R}^{D_1}, \mathbb{R}^{D_2}, \dots, \mathbb{R}^{D_M}\} \rightarrow \mathbb{R}$  which takes in a data point  $\mathbf{x}_i$  and outputs a predicted value  $\hat{y}_i$ .

### 3.2. Composite GPs

A Gaussian process (GP) describes a distribution over functions (Williams & Rasmussen, 2006). A key property of GP is that it is completely defined by a mean function  $\mu(\mathbf{x})$  and a kernel function  $K(\mathbf{x}, \mathbf{x}')$  where  $\mathbf{x}$  and  $\mathbf{x}'$  represent different samples from the training dataset. The mean function  $\mu(\mathbf{x})$  is often assumed to be zero for simplicity. In that case, the outcome function is

$$f(\mathbf{x}) \sim \mathcal{GP}(0, K(\mathbf{x}, \mathbf{x}')). \quad (1)$$

Any finite subset of random variables has a multivariate Gaussian distribution with mean  $\mathbf{0}$  and kernel matrix  $\mathbf{K}$  whose entries can be calculated as  $K_{ij} = K(\mathbf{x}_i, \mathbf{x}_j)$  where  $1 \leq i, j \leq N$ . In many situations, the full kernel function is built by a composite kernel by combining simple kernels through addition  $K^{\text{comp}}(\mathbf{x}, \mathbf{x}') = K_1(\mathbf{x}, \mathbf{x}') + K_2(\mathbf{x}, \mathbf{x}')$  or multiplication  $K^{\text{comp}}(\mathbf{x}, \mathbf{x}') = K_1(\mathbf{x}, \mathbf{x}')K_2(\mathbf{x}, \mathbf{x}')$  (Duvenaud, 2014). A useful property that ICK exploits is that  $K_1$  and  $K_2$  can take different subparts of  $\mathbf{x}$  as their inputs. For example,  $K^{\text{comp}}(\mathbf{x}, \mathbf{x}') = K_1(\mathbf{x}^{(1)}, \mathbf{x}^{(1)'}) + K_2(\mathbf{x}^{(2)}, \mathbf{x}^{(2)'})$  or  $K^{\text{comp}}(\mathbf{x}, \mathbf{x}') = K_1(\mathbf{x}^{(1)}, \mathbf{x}^{(1)'})K_2(\mathbf{x}^{(2)}, \mathbf{x}^{(2)'})$ .

### 3.3. Correspondence between GPs and NNs

Neal (Neal, 1996) proved that a single-hidden layer network with infinite width is *exactly equivalent* to a GP over data indices  $i = 1, 2, \dots, N$  under the assumption that the weight and bias parameters of the hidden layer are i.i.d. Gaussian with zero mean. This statement was then extended to deep NNs (Lee et al., 2017; Matthews et al., 2018) and convolutional NNs (Garriga-Alonso et al., 2018). Specifically, let  $\mathbf{z} = f_{\text{NN}}(\mathbf{x}^{(1)}) : \mathbb{R}^{D_1} \rightarrow \mathbb{R}^p$  be the latent representation extracted from  $\mathbf{x}^{(1)}$  where  $p$  is the dimension of the extracted representation and  $f_{\text{NN}}$  is a neural network with zero-mean i.i.d. parameters and continuous activation function  $\phi$  which satisfies the linear envelope property

$$|\phi(u)| \leq c + m|u| \quad \forall u \in \mathbb{R}, \quad (2)$$

if there exists  $c, m \geq 0$ . This includes many standard nonlinearities. The  $k^{\text{th}}$  entry of this representation will converge in distribution to a NN-implied GP in the infinite width limit

$$f_{\text{NN}}(\mathbf{x}^{(1)})_k \xrightarrow{d} \mathcal{GP}\left(0, K_{\text{NN}}(\mathbf{x}^{(1)}, \mathbf{x}^{(1)'})\right). \quad (3)$$

Here  $K_{\text{NN}}$  in Equation 3 denotes the covariance function of the equivalent GP as the width of  $f_{\text{NN}}$  goes to infinity and can be computed numerically in a recursive manner (Lee et al., 2017). That is to say, the  $k^{\text{th}}$  component  $z_k$  of

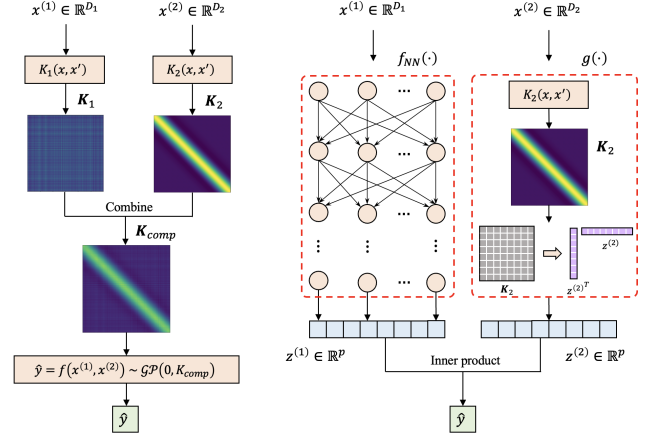


Figure 1. Given data containing 2 sources of information  $\mathbf{x}^{(1)}$  and  $\mathbf{x}^{(2)}$ , we can process the data using either (Left) a composite Gaussian process regression (GPR) model or (Right) our ICK framework where  $\mathbf{x}^{(1)}$  is processed with a neural network  $f_{\text{NN}}(\cdot)$  and  $\mathbf{x}^{(2)}$  is processed with  $g(\cdot)$  where  $g(\cdot)$  consists of a kernel function  $K_2$  and some transformation which maps the kernel matrix  $\mathbf{K}_2$  into the latent space.

the representation extracted by the network has zero mean  $\mathbb{E}_{p(\theta^{(1)})} [z_{ik}^{(1)}] = 0$  for all  $i = 1, 2, \dots, N$  where  $\theta$  represents the network parameters. The covariance between  $z_{ik}^{(1)}$  and  $z_{jk}^{(1)}$  for different data indices  $i, j = 1, 2, \dots, N$  can be approximated as  $\text{cov}(z_{ik}^{(1)}, z_{jk}^{(1)}) = \mathbb{E}_{p(\theta^{(1)})} [z_{ik}^{(1)} z_{jk}^{(1)}] \approx K_{\text{NN}}(\mathbf{x}_i^{(1)}, \mathbf{x}_j^{(1)})$  where  $\mathbf{x}_i^{(1)}$  and  $\mathbf{x}_j^{(1)}$  are the corresponding inputs in case the network width is finite.

## 4. Implicit Composite Kernel

We show the structure of a composite GPR model and our ICK framework in Figure 1. To make the illustration clear, we limit ourselves to data with information from 2 different sources  $\mathbf{x} = \{\mathbf{x}^{(1)}, \mathbf{x}^{(2)}\}$  where  $\mathbf{x}^{(1)}$  is high-dimensional and  $\mathbf{x}^{(2)}$  is low-dimensional (i.e.  $D_1 \gg D_2$ ) with some known relationship with the target  $y$ . We are inspired by composite GPR, which computes 2 different kernel matrices  $\mathbf{K}_1$  and  $\mathbf{K}_2$  and then combines them into a single composite kernel matrix  $\mathbf{K}^{\text{comp}}$ . However, as discussed before, it is more suitable to use a NN to learn from the high dimensional information  $\mathbf{x}^{(1)}$ . In our ICK framework, we process  $\mathbf{x}^{(1)}$  with a NN  $f_{\text{NN}}(\cdot) : \mathbb{R}^{D_1} \rightarrow \mathbb{R}^p$  and  $\mathbf{x}^{(2)}$  with a mapping  $g(\cdot) : \mathbb{R}^{D_2} \rightarrow \mathbb{R}^p$ , which consists of a kernel function  $K_2$  followed by a kernel-to-latent-space transformation (described in Section 4.2), resulting in two latent representations  $\mathbf{z}^{(1)}, \mathbf{z}^{(2)} \in \mathbb{R}^p$ . Then, we make a prediction  $\hat{y}$  by doing an inner product between these two representations  $\hat{y} = f_{\text{NN}}(\mathbf{x}^{(1)}) \cdot g(\mathbf{x}^{(2)})$ . Finally, the parameters of both the NN and the kernel function are learned via gradient-

based optimization methods (Bottou et al., 2018).

In the sections below, we first show the relationship between ICK and a composite GPR model with a multiplicative kernel *a priori* in Section 4.1, which is used to motivate the model form. We then show how we implement the kernel-to-latent-space transformation in Section 4.2. We then use the idea from Lee et al. (Lee et al., 2017) that finite-width NNs trained with stochastic gradient descent (SGD) mimic Bayesian inference on a GP. However, without Bayesian formulation on the NN and kernel function parameters, the prediction  $\hat{y}$  can only be viewed as a *posterior sample* corresponding to an *approximate* GP prior. To enable a full GP posterior *approximation* for ICK, we adopt a sample-then-optimize procedure (Matthews et al., 2017) to formulate an ensemble algorithm, as elaborated in Section 4.3.

#### 4.1. Resemblance between Composite GPR and ICK

We will analytically prove the following theorem for data with information from 2 different sources  $\mathbf{x} = \{\mathbf{x}^{(1)}, \mathbf{x}^{(2)}\}$  for clarity, and we note this theorem can be straightforwardly extended to  $M > 2$ .

**Theorem 4.1.** *Let  $f_{NN} : \mathbb{R}^{D_1} \rightarrow \mathbb{R}^p$  be a NN function with random weights and  $g : \mathbb{R}^{D_2} \rightarrow \mathbb{R}^p$  be a mapping function, and define an inner product between the representations  $\hat{y} = f_{ICK}(\mathbf{x}^{(1)}, \mathbf{x}^{(2)}) = f_{NN}(\mathbf{x}^{(1)}) \cdot g(\mathbf{x}^{(2)}) = \mathbf{z}^{(1)T} \mathbf{z}^{(2)}$ . Then  $f_{ICK}$  will converge in distribution to a GP*

$$f_{ICK} \xrightarrow{d} \mathcal{GP}\left(0, K_{NN}^{(1)}(\mathbf{x}^{(1)}, \mathbf{x}^{(1)'}) K^{(2)}(\mathbf{x}^{(2)}, \mathbf{x}^{(2)'})\right), \quad (4)$$

if  $f_{NN}$  is a neural network with zero-mean i.i.d. parameters and continuous activation function  $\phi$  which satisfies the linear envelope property in Equation 2 and  $g$  includes the following deterministic kernel-to-latent-space transformation for all  $1 \leq i, j \leq N$

$$K^{(2)}(\mathbf{x}_i^{(2)}, \mathbf{x}_j^{(2)}) \approx \mathbf{z}_i^{(2)T} \mathbf{z}_j^{(2)} = g(\mathbf{x}_i^{(2)})^T g(\mathbf{x}_j^{(2)}), \quad (5)$$

where  $K_{NN}^{(1)}$  is a NN-implied kernel and  $K^{(2)}$  is any valid kernel of our choice.

To prove Theorem 1, we first make the assumption below.

**Assumption 4.2.** For latent representations  $\mathbf{z}_i^{(1)}$  and  $\mathbf{z}_j^{(1)}$  extracted from different data points  $\mathbf{x}_i$  and  $\mathbf{x}_j$  where  $i \neq j$ , the interactions between different entries of  $\mathbf{z}_i^{(1)}$  and  $\mathbf{z}_j^{(1)}$  can be reasonably ignored. In other words, let  $\theta^{(1)}$  be the parameters of the neural network which takes in  $\mathbf{x}^{(1)}$  and outputs  $\mathbf{z}^{(1)}$ , we have  $\mathbb{E}_{p(\theta^{(1)})} [z_{ik}^{(1)} z_{jl}^{(1)}] = 0$  for all  $k \neq l$ .

A detailed discussion of Assumption 4.2 and its reasonableness is provided in Appendix A.2. With Assumption 4.2, let  $\Theta = \{\theta^{(1)}, \theta^{(2)}\}$  represent the parameters of ICK, we

can calculate the covariance between  $\hat{y}_i$  and  $\hat{y}_j$  for different data indices  $i \neq j$ :

$$\begin{aligned} \text{cov}(\hat{y}_i, \hat{y}_j) &= \mathbb{E}_{p(\Theta)} [\hat{y}_i \hat{y}_j] - \mathbb{E}_{p(\Theta)} [\hat{y}_i] \mathbb{E}_{p(\Theta)} [\hat{y}_j] \end{aligned} \quad (6)$$

$$= \mathbb{E}_{p(\Theta)} \left[ \left( \sum_{k=1}^p z_{ik}^{(1)} z_{ik}^{(2)} \right) \left( \sum_{l=1}^p z_{jk}^{(1)} z_{jk}^{(2)} \right) \right] \quad (7)$$

$$= \mathbb{E}_{p(\Theta)} \left[ \sum_{k=1}^p \sum_{l=1}^p z_{ik}^{(1)} z_{jl}^{(1)} z_{ik}^{(2)} z_{jl}^{(2)} \right] \quad (8)$$

$$= \mathbb{E}_{p(\Theta)} \left[ \sum_{k=1}^p z_{ik}^{(1)} z_{jk}^{(1)} z_{ik}^{(2)} z_{jk}^{(2)} \right] \quad (9)$$

$$= \sum_{k=1}^p \mathbb{E}_{p(\theta^{(1)})} [z_{ik}^{(1)} z_{jk}^{(1)}] \mathbb{E}_{p(\theta^{(2)})} [z_{ik}^{(2)} z_{jk}^{(2)}] \quad (10)$$

$$\approx K_{NN}^{(1)}(\mathbf{x}_i^{(1)}, \mathbf{x}_j^{(1)}) \sum_{k=1}^p \mathbb{E}_{p(\theta^{(2)})} [z_{ik}^{(2)} z_{jk}^{(2)}]. \quad (11)$$

Here, from Equation 6 to Equation 7, we use the statement  $\mathbb{E}_{p(\theta^{(1)})} [z_{ik}^{(1)}] = 0$  in Section 3.3 and  $\theta^{(1)} \perp \theta^{(2)}$ , which leads to  $\mathbb{E}_{p(\Theta)} [\hat{y}_i] = \mathbb{E}_{p(\Theta)} [\hat{y}_j] = 0$ . From Equation 8 to Equation 9, we get rid of all the cross terms under Assumption 4.2 and  $\theta^{(1)} \perp \theta^{(2)}$ . Specifically, we have  $\mathbb{E}_{p(\Theta)} [z_{ik}^{(1)} z_{jl}^{(1)} z_{ik}^{(2)} z_{jl}^{(2)}] = \mathbb{E}_{p(\theta^{(1)})} [z_{ik}^{(1)} z_{jl}^{(1)}] \mathbb{E}_{p(\theta^{(2)})} [z_{ik}^{(2)} z_{jl}^{(2)}] = 0$  for all  $k \neq l$ . From Equation 9 to Equation 10, we again make use of  $\theta^{(1)} \perp \theta^{(2)}$ . From Equation 10 to Equation 11, we use the statement  $\mathbb{E}_{p(\theta^{(1)})} [z_{ik}^{(1)} z_{jk}^{(1)}] \approx K_{NN}(\mathbf{x}_i^{(1)}, \mathbf{x}_j^{(1)})$  from Section 3.3. If the kernel-to-latent-space transformation in  $g(\cdot)$  is *deterministic*, we can remove the expectation sign from the summation term in Equation 11 and the covariance can be further expressed as

$$\begin{aligned} \text{cov}(\hat{y}_i, \hat{y}_j) &\approx K_{NN}^{(1)}(\mathbf{x}_i^{(1)}, \mathbf{x}_j^{(1)}) \left( \mathbf{z}_i^{(2)T} \mathbf{z}_j^{(2)} \right) \\ &= K_{NN}^{(1)}(\mathbf{x}_i^{(1)}, \mathbf{x}_j^{(1)}) K^{(2)}(\mathbf{x}_i^{(2)}, \mathbf{x}_j^{(2)}), \end{aligned} \quad (12)$$

which means that  $\hat{y}$  approximately follows a GP with a multiplicative composite kernel  $K^{\text{comp}}(\mathbf{x}_i, \mathbf{x}_j) = K_{NN}^{(1)}(\mathbf{x}_i^{(1)}, \mathbf{x}_j^{(1)}) K^{(2)}(\mathbf{x}_i^{(2)}, \mathbf{x}_j^{(2)})$  *a priori*. This serves as a concise proof of Theorem 1. We also give a more detailed proof Appendix A.

#### 4.2. Kernel-to-latent-space Transformation

We now show how we can construct an appropriate mapping  $g(\cdot)$  that approximately satisfies the assumed form of (5) and is used in the derivation of ICK from (11) to (12). Here we adopt two methods, Nyström approximation and Random Fourier Features (RFF), to map the kernel matrix into the latent space. Below, we give the formulations and results for the Nyström method, and give the methods and results for RFF in Appendix B. According to Yang et al. (Yang et al., 2012), the Nyström method will yield much better

**Algorithm 1** Implicit Composite Kernel-Nyström (ICKy)

**Input:** data  $\mathbf{X} = \{\mathbf{x}_i^{(1)}, \mathbf{x}_i^{(2)}\}_{i=1}^N$ , targets  $\mathbf{y} = [y_i]_{i=1}^N$ ,  $f_{\text{NN}}, \boldsymbol{\theta}^{(1)}, K^{(2)}, \boldsymbol{\theta}^{(2)}$ , learning rate  $\beta$   
 Sample a total of  $N_B$  minibatches  $\{\mathbf{X}_B, \mathbf{y}_B\}_{B=1}^{N_B}$   
**for**  $B$  from 1 to  $N_B$  **do**  
     **for**  $\mathbf{x}_i^{(1)}, \mathbf{x}_i^{(2)}$  in  $\mathbf{X}_B, i = 1, \dots, n_B$  **do**  
          $\mathbf{z}_i^{(1)} = f_{\text{NN}}(\mathbf{x}_i^{(1)})$   
         Define inducing points  $\hat{\mathbf{x}}_1^{(2)}, \dots, \hat{\mathbf{x}}_p^{(2)}$   
         Compute  $\mathbf{K}_p$ :  $(\mathbf{K}_p)_{jk} = K^{(2)}(\hat{\mathbf{x}}_j^{(2)}, \hat{\mathbf{x}}_k^{(2)})$   
         Do Cholesky decomposition  $(\mathbf{K}_p)^{-1} = \mathbf{U}^T \mathbf{U}$   
         Compute  $\mathbf{K}_{np}$ :  $(\mathbf{K}_{np})_{jk} = K^{(2)}(\mathbf{x}_j^{(2)}, \hat{\mathbf{x}}_k^{(2)})$   
          $\mathbf{z}_i^{(2)} = \mathbf{U}(\mathbf{K}_{np}^T)_{:,i}$   
          $\hat{\mathbf{y}}_i = \mathbf{z}_i^{(1)T} \mathbf{z}_i^{(2)}$   
     **end for**  
      $\hat{\mathbf{y}}_B = \text{concat}(\hat{\mathbf{y}}_1, \dots, \hat{\mathbf{y}}_{n_B})$   
     Compute loss  $\mathcal{L} = \mathcal{L}(\mathbf{y}_B, \hat{\mathbf{y}}_B)$   
      $\boldsymbol{\theta}^{(1)} \leftarrow \boldsymbol{\theta}^{(1)} - \beta \nabla_{\boldsymbol{\theta}^{(1)}} \mathcal{L}$   
      $\boldsymbol{\theta}^{(2)} \leftarrow \boldsymbol{\theta}^{(2)} - \beta \nabla_{\boldsymbol{\theta}^{(2)}} \mathcal{L}$   
**end for**  
**Return:** Predictions  $\hat{\mathbf{y}}$  and updated parameters  $\boldsymbol{\theta}^{(1)}, \boldsymbol{\theta}^{(2)}$

performance than RFF if there exists a large gap in the eigen-spectrum of the kernel matrix. In our applications, we also observe a large eigen-gap (see details in Appendix C) and Nyström method does generalize much better than RFF. We name our framework with Nyström method and random Fourier Features ICKy and ICKr, respectively.

#### 4.2.1. NYSTRÖM METHOD

The main idea of Nyström method (Williams & Seeger, 2000) is to approximate the kernel matrix  $\mathbf{K} \in \mathbb{R}^{N \times N}$  with a much smaller low-rank matrix  $\mathbf{K}_q \in \mathbb{R}^{q \times q}$  where  $q \ll N$  so both the computational and space complexity of kernel learning can be significantly reduced, yielding

$$\mathbf{K} \approx \hat{\mathbf{K}} = \mathbf{K}_{nq} \mathbf{K}_q^{-1} \mathbf{K}_{nq}^T. \quad (13)$$

The entries of  $\mathbf{K}_q$  and  $\mathbf{K}_{nq}$  can be calculated as  $(\mathbf{K}_q)_{ij} = K(\hat{\mathbf{x}}_i, \hat{\mathbf{x}}_j), i, j \in \{1, 2, \dots, q\}$  and  $(\mathbf{K}_{nq})_{ij} = K(\mathbf{x}_i, \hat{\mathbf{x}}_j), i \in \{1, 2, \dots, N\}, j \in \{1, 2, \dots, q\}$ , respectively.  $\mathbf{x}$  represents the original data points and  $\hat{\mathbf{x}}$  represents pre-defined inducing points (or pseudo-inputs (Snelson & Ghahramani, 2005)). In our study, these inducing points are chosen by defining an evenly spaced vector over the range of original data points. By performing Cholesky decompo-

sition  $\mathbf{K}_q^{-1} = \mathbf{U}^T \mathbf{U}$ , where  $\mathbf{U} \in \mathbb{R}^{q \times q}$ ,  $\hat{\mathbf{K}}$  is expressed

$$\begin{aligned} \hat{\mathbf{K}} &= \mathbf{K}_{nq} \mathbf{K}_q^{-1} \mathbf{K}_{nq}^T = \mathbf{K}_{nq} \mathbf{U}^T \mathbf{U} \mathbf{K}_{nq}^T \\ &= (\mathbf{U} \mathbf{K}_{nq}^T)^T (\mathbf{U} \mathbf{K}_{nq}^T). \end{aligned} \quad (14)$$

Therefore, if we set  $q = p$ , then we can use  $\mathbf{z}_i \triangleq \mathbf{U}(\mathbf{K}_{np}^T)_{:,i}$  as a kernel-to-latent-space transformation because each element in  $\mathbf{K}$  approximately satisfies (5) as stated in Theorem 1:  $K(\mathbf{x}_i, \mathbf{x}_j) = K_{ij} \approx \hat{K}_{ij} = \mathbf{z}_i^T \mathbf{z}_j$ . Conveniently, modern deep learning frameworks can propagate gradients through the Cholesky operation, making it straightforward to update the kernel parameters with gradient methods. Note that as we increase the number of inducing points  $p$ , the approximation error between  $\mathbf{K}$  and  $\hat{\mathbf{K}}$  decreases. However, it is not recommended to set  $p$  very large as updating the Cholesky decomposition requires  $\mathcal{O}(p^3)$ . The empirical impact of  $p$  on computational time and performance is shown in Appendix D. In our experiments, only mild values of  $p$  are necessary and the impact on computational is relatively small. The full training procedure of ICKy is shown in Algorithm 1.

#### 4.3. Ensemble Formulation of ICK

We adopt a sample-then-optimize approach (Matthews et al., 2017) to construct a deep ensemble posterior approximation for ICK. There are several ways to enable GP posterior interpretation for a deep ensemble trained with SGD. Specifically, let the final layer of each baselearner NN be  $C$ -dimensional and denote the deep ensemble as  $F = \{f_{n_e}\}_{n_e=1}^{N_e}$ , where  $f_{n_e}$  is a baselearner NN and  $N_e$  is the total number of baselearners in the ensemble. After training, each  $f_{n_e}$  can be viewed as i.i.d. samples from a multi-output GP posterior with kernel function  $K_F$  in the infinite width limit and the ensemble  $F$  thus represents  $N_e$  independent draws from the GP posterior, where  $K_F$  can be either the *Neural Network Gaussian Process* (NNGP) kernel (Lee et al., 2017) if we make only the last layer trainable or the *Neural Tangent Kernel* (NTK) (He et al., 2020; Jacot et al., 2018) if we add a randomized and untrainable function to each baselearner.

This deep ensemble mechanism can be easily applied to ICKy. Specifically, the final prediction of ICKy  $\hat{\mathbf{y}} = f_{\text{ICKy}}(\mathbf{x}^{(1)}, \mathbf{x}^{(2)})$  can be viewed as a weighted sum of  $\hat{\mathbf{y}} = \sum_{k=1}^p \alpha_k \mathbf{z}_k^{(1)}$  where  $\alpha_k = \mathbf{z}_k^{(2)T} \mathbf{g}(\mathbf{x}^{(2)})_k$ . Hence, if we construct an ensemble of ICKy,  $F_{\text{ICKy}} = \{f_1, \dots, f_{N_e}\}$  (as shown in Algorithm 2), and  $f_{\text{NN}}$  is appropriately initialized for all baselearners  $f_s \in F_{\text{ICKy}}, s = 1, \dots, N_e$ , then all trained baselearners in  $F_{\text{ICKy}}$  can be approximately viewed as i.i.d. posterior samples from a single-output GP with a multiplicative kernel  $K_F K^{(2)}$ .  $K_F$  will either be an NNGP or an NTK and  $K^{(2)}$  comes from our defined kernel. If the parameters of  $f_{\text{NN}}$  (i.e.  $\boldsymbol{\theta}^{(1)}$ ) are independently drawn from a zero-mean Gaussian and are fixed except the last layer (as

**Algorithm 2** ICKy Ensemble

**Input:** data  $\mathbf{X} = \{\mathbf{x}_i^{(1)}, \mathbf{x}_i^{(2)}\}_{i=1}^N$ , targets  $\mathbf{y} = [y_i]_{i=1}^N$ , ensemble  $F_{\text{ICKy}} = \{f_1, \dots, f_{N_e}\}$  where each function in  $F$  consists of  $f_{\text{NN}}, K^{(2)}$  with parameters  $\theta^{(1)}, \theta^{(2)}$ , respectively

**for**  $s = 1, \dots, N_e$  **do**

    Apply proper initialization strategy to  $f_s$

    Perform Algorithm 1 on function  $f_s$

**end for**

**Return:**

Predictive mean  $\hat{\mu} = \frac{1}{N_e} \sum_{s=1}^{N_e} f_s(\mathbf{X})$

Predictive variance  $\hat{\sigma}^2 = \frac{1}{N_e} \sum_{s=1}^{N_e} (f_s(\mathbf{X}) - \hat{\mu})^2$

Updated parameters  $\theta^{(1)}, \theta^{(2)}$  for all functions  $f$  in  $F_{\text{ICKy}}$

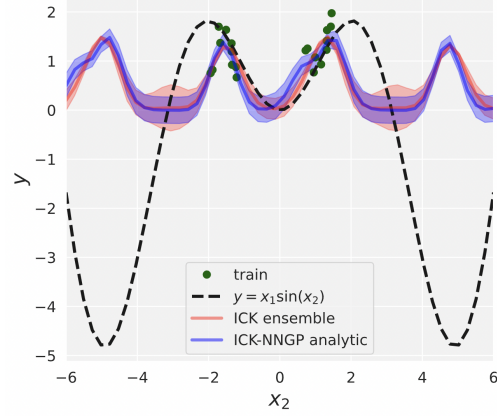


Figure 2. Predictive distribution from ICKy ensemble and its GP posterior counterpart on a 1D regression task

specified by Lee et al. (Lee et al., 2019)) for all baselearners in the ensemble, this would correspond to an NNGP. A more detailed proof of this argument can be found in Appendix E.

To verify our argument, we train an ICKy ensemble  $F_{\text{ICKy}}$  containing 300 baselearners with SGD on the same 1D regression task as provided by He et al. (He et al., 2020) and compare the predictive distribution to its GP posterior counterpart based on the NNGP implementation in the *neural-tangents* (Novak et al., 2020) package. The GP posterior has zero mean and kernel function  $K_{\text{NNGP}}K^{(2)}$ , where  $K_{\text{NNGP}}$  is the corresponding NNGP kernel of  $f_{\text{NN}}$  and  $K^{(2)}$  is the chosen kernel function for the mapping  $g$  in the ICKy ensemble. Here,  $K^{(2)}$  is set as an *exponential-sine-squared* kernel with period  $T = 2\pi$ . As shown in Figure 2, the predictive distribution of ICKy ensemble is very close to the analytic GP posterior, demonstrating the *approximate* equivalence between the two models (see Appendix L for more evidence). Alternative strategies can also be used to approximate a GP posterior with a multiplicative kernel between NTK and  $K^{(2)}$ .

## 5. Experimental Results

We evaluate ICKy on 3 different data sets: a synthetic data set <sup>1</sup>, a remote sensing data set <sup>2</sup>, and a worker productivity data set <sup>1</sup> obtained from UCI Machine Learning Repository (Dua & Graff, 2017). In all 3 experiments, our ICKy framework only consists of 2 kernels (i.e.  $M = 2$ ), one NN-implied kernel and one chosen kernel function with trainable parameters. To verify that ICKy can work with more than 2 kernels, we create another synthetic data set with 3 kernels and show the results in Appendix F. The implementation details of all the experiments in this section are provided in Appendix G and the data accessibility and restrictions are provided in Appendix H. Besides regression tasks, we also elaborate how ICK can adapt to classification

tasks in Appendix I.

### 5.1. Synthetic Data

To verify that ICKy can simulate sampling from a GP with *multiplicative kernel*, we create a synthetic data set  $y \sim \mathcal{GP}(0, K_1 K_2)$  containing 3000 data points where  $\mathbf{x}^{(1)} \in [0, 1]$  is the input for the linear kernel  $K_1$  and  $\mathbf{x}^{(2)} \in [0, 2]$  is the input for the *spectral mixture* kernel (Wilson & Adams, 2013)  $K_2$  with 2 components. The data set is first randomly shuffled and then divided into train and test set with a 50:50 ratio. With ICKy, we process  $\mathbf{x}^{(1)}$  with a single-hidden-layer NN and  $\mathbf{x}^{(2)}$  with a spectral mixture kernel function.

We then compare ICKy with two models: a multi-layer perceptron (MLP) applied to the concatenated features and a novel multi-layer perceptron-random forest (MLP-RF) joint model employed by Zheng et al. (2021), where MLP learns from  $\mathbf{x}^{(1)}$  and RF learns from  $\mathbf{x}^{(2)}$ . We believe MLP-RF serves as a good benchmark model as it is a joint model with similar architecture to our ICKy framework. To see how ICKy simulates the spectral mixture kernel, we plot only  $\mathbf{x}^{(2)}$  against the predicted value of  $y$  as shown in Figure 3. As can be seen from the figure, plain MLP only captures the linear trend. MLP-RF only captures the mean of the spectral mixture components. In contrast, our ICKy framework captures both the mean and the variance of the spectral mixture kernel. To test the robustness of ICKy, we also conduct experiments on another synthetic data set in Appendix J to confirm that ICKy can simulate an *additive kernel*.

<sup>1</sup>Code for synthetic and worker productivity data: [https://anonymous.4open.science/r/ICK\\_NNGP-FF83/](https://anonymous.4open.science/r/ICK_NNGP-FF83/).

<sup>2</sup>Code for remote sensing and ICKy ensemble: <https://anonymous.4open.science/r/ICK-8F87/>.

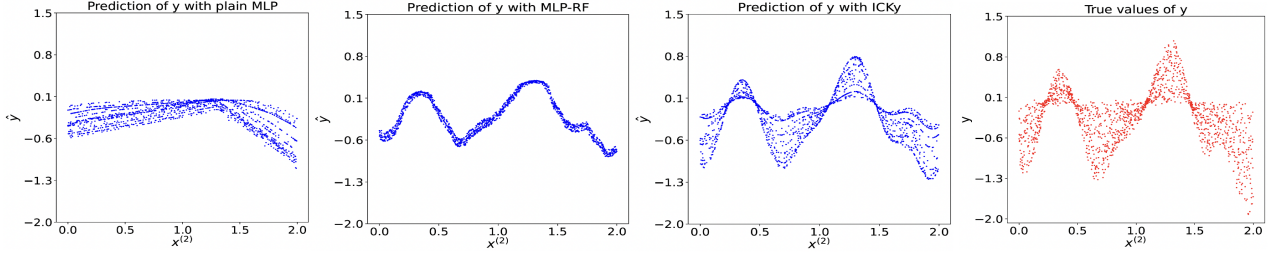


Figure 3. Prediction of  $y \sim \mathcal{GP}(0, K_1 K_2)$ , where  $x^{(1)}$  is input to a linear kernel  $K_1$  and  $x^{(2)}$  is input to a spectral mixture kernel  $K_2$ . We plot  $x^{(2)}$  against the predicted  $y$ . We show results from a plain MLP (left), MLP-RF (middle left), and ICKy framework (middle right), and we compare to the true values of  $y$  (right).

## 5.2. Remote Sensing Data

We believe ICKy will be particularly useful for remote sensing applications. In this experiment, we collect remote sensing data from 51 air quality monitoring (AQM) stations located in the National Capital Territory (NCT) of Delhi and its satellite cities over the period from January 1, 2018 to June 30, 2020 (see Appendix H for notes on data availability). Each data point  $x = \{x, t\}$  contains 2 sources of information: a three-band natural color (red-blue-green) satellite image  $x$  as the high-dimensional information and the corresponding timestamp as the low-dimensional information. Note that we convert the timestamps into numerical values  $t$  (where the day 2018-01-01 corresponds to  $t = 0$ ) before feeding them into the models. Our goal is to predict the ground-level  $\text{PM}_{2.5}$  concentration  $\hat{y} = f(x, t)$  using both sources of information.

We split the train, validation, and test data set based on  $t$ . Specifically, we use all the data points with  $t < 365$  for training,  $365 \leq t < 500$  for validation, and  $t \geq 500$  for testing. As  $\text{PM}_{2.5}$  varies with time on a yearly basis, we use an *exponential-sine-squared* kernel with a period of  $T = 365$  (days) to process the low-dimensional information  $t$ . The satellite images are processed with a CNN. The results of ICKy are then compared with 2 benchmarks as shown in Table 1: a Convolutional Neural Network-Random Forest (CNN-RF) joint model (Zheng et al., 2021; 2020) (similar to the MLP-RF model in Section 5.1, where RF learns the temporal variation of  $\text{PM}_{2.5}$  and CNN captures the spatial variation of  $\text{PM}_{2.5}$  from satellite images) and a *carefully designed* CNN-RF model that maps  $t$  into two new features,  $\sin(2\pi t/365)$  and  $\cos(2\pi t/365)$ , to explicitly model seasonality, which we call Seasonal CNN-RF.

We note that the inner product operation in ICK is similar in mathematical structure to attention-based mechanisms (Vaswani et al., 2017), which are popular in many deep learning frameworks. Therefore, we introduce 2 variants of ICKy and compare them with another 4 benchmarks where the CNN is replaced by an attention-based mechanism based off of a Vision Transformer (ViT) (Dosovitskiy et al., 2020)

and DeepViT (Zhou et al., 2021) architectures. These models include ViT-RF, Seasonal ViT-RF, Seasonal DeepViT-RF, and Seasonal MAE-ViT-RF, where ViT is pre-trained by a Masked Autoencoder (He et al., 2022). “Seasonal” here denotes that we use the transformed periodic representation defined above. We note that we are unaware of Vision Transformers being used in this manner, and we want to evaluate whether it is the model structure or the prior information that is improving the results. Hence, these attention-based models, while not a primary contribution, are novel and represent a good-faith effort to define models with similar forms. As displayed in Table 1, both standard CNN-RF and ViT-RF models yields very large errors on predicting  $\text{PM}_{2.5}$  values. After including seasonality, CNN-RF performs significantly better and shares similar predictive performance with CNN-ICKy. After replacing CNN with ViT, we observe slight improvement in both RF-joint models (especially when pre-trained by MAE) and ICKy variants. Among all the models we present here, ViT-ICKy and DeepViT-ICKy achieve the highest correlation and the smallest prediction error, respectively. To evaluate the uncertainty calibration capability of ICKy, we construct **ICKy ensembles** by following Algorithm 2 and compare them with ensemble formulations of RF-joint model benchmarks. We use an evaluation criterion called Mean Standardized Log Loss (MSLL) (Williams & Rasmussen, 2006),

$$\text{MSLL} = \frac{1}{2N} \sum_{i=1}^N \left( \log(2\pi\hat{\sigma}_i^2) + \frac{(y - \hat{\mu}_i)^2}{\hat{\sigma}_i^2} \right), \quad (15)$$

where  $\hat{\mu}_i$  and  $\hat{\sigma}_i^2$  represents the predictive mean and variance for the  $i^{\text{th}}$  data point, respectively. From Table 1, it can be observed that CNN-ICKy ensemble achieves the smallest MSLL. In addition, we realize ViT-based ICKy variants yield very large MSLL as they make predictions which are far from the true  $\text{PM}_{2.5}$  labels with high confidence (i.e. small variance). We provide details and possible explanations in Appendix K.

## 5.3. Worker Productivity Data

To see if our ICKy framework generalizes to other domains, we acquire another data set containing the normalized pro-

Table 1. Correlation and error statistics of ICKy and other joint deep models with both convolutional and attention-based architectures on the PM<sub>2.5</sub> forecasting task. “S.” denotes seasonal variants.

	R <sub>Spear</sub>	RMSE	MAE	MSLL
CNN-RF	0.00	194.63	185.83	-
ViT-RF	0.07	190.82	181.63	-
S. CNN-RF	0.62	53.36	39.38	96.77
S. ViT-RF	0.66	56.45	41.73	14.69
S. Deep-ViT-RF	0.65	56.36	42.46	17.63
S. MAE-ViT-RF	0.67	53.87	40.78	31.09
CNN-ICKy	0.62	53.46	39.76	<b>10.92</b>
ViT-ICKy	<b>0.68</b>	56.56	41.41	12208
DeepViT-ICKy	0.66	<b>52.41</b>	<b>35.93</b>	38220

ductivity and corresponding features of garment workers from the UCI Machine Learning Repository. Imran et al. (Al Imran et al., 2019) employed a dense MLP with 2 hidden layers to predict the worker productivity with collected features such as date, team number, targeted productivity, etc. To test our ICKy framework, we separate out the *date* and use it as the low-dimensional information. The rest of the features (excluding the temporal information) are then concatenated together to serve as the high-dimensional information. Observing that the *daily averaged* worker productivity has an approximate *monthly trend*, we again use an *exponential-sine-squared* kernel. The network architecture of ICKy is the same as that of the two-hidden-layer MLP benchmark. To demonstrate the strength of ICKy compared to other methods that equip NNs with GPs, we also add 2 additional benchmarks here: a Gaussian Neural Process (GNP) (Bruinsma et al., 2021) and an Attentive Gaussian Neural Process (AGNP) (Kim et al., 2019). Based on the results shown in Table 2, ICKy has the best performance when the period parameter of the kernel is set to be  $T = 30$  (days) and it outperforms both MLP and NP benchmarks by almost **one order of magnitude**. When we set  $T = 2$  or  $T = 7$ , this improvement is less significant, which aligns with our initial observation that the daily averaged productivity has a monthly seasonal trend. It is also worth noting that the GNP benchmarks here yield larger errors than MLPs. A possible explanation is that GNP does not allow explicit assignment of a stationary kernel (as the kernel models a posterior covariance) so it is hard for GNP to identify specific patterns in the data such as seasonality without being given the pattern *a priori*.

## 6. Discussion

**Efficiency and Flexibility of ICK** Compared to exact composite GP models which scale  $\mathcal{O}(N^3)$ , the training process of our ICK framework is more efficient as it leverages standard backpropagation to learn both the parameters of NN and the kernel function. Besides efficiency, our ICK

Table 2. Prediction error of actual worker productivity on the test data set with ICKy and other benchmark models (MLPs and NPs)

	MSE $\downarrow$ ( $\times 10^{-3}$ )	MAE $\downarrow$ ( $\times 10^{-2}$ )
MLP	20.16 $\pm$ 1.26	9.93 $\pm$ 0.36
Cyclic MLP	20.97 $\pm$ 1.98	10.16 $\pm$ 0.77
GNP	57.25 $\pm$ 4.31	19.39 $\pm$ 0.94
AGNP	43.11 $\pm$ 5.95	14.38 $\pm$ 0.88
ICKy, $T = 2$	3.43 $\pm$ 1.42	4.85 $\pm$ 1.00
ICKy, $T = 7$	0.44 $\pm$ 0.13	1.43 $\pm$ 0.15
ICKy, $T = 30$	<b>0.31 <math>\pm</math> 0.09</b>	<b>1.17 <math>\pm</math> 0.14</b>

framework is more flexible compared to other joint models (i.e. BNNs and CNN-RF). To be specific, the BNNs implemented by Pearce et al. (Pearce et al., 2020) cannot simulate complicated kernels such as the spectral mixture kernel we use in Section 5.1. The CNN-RF joint model implemented by Zheng et al. (Zheng et al., 2021) requires us to carefully design the input pre-processing procedure. There is a potential concern that ICKy may run into computational challenges when a large number of inducing points are required. This was not a problem in our experiments, but in large scale models this could be tackled by considering conjugate gradient methods, which have been recently popular in GP inference (Gardner et al., 2018).

**Limitations** A limitation of ICK lies in our method of combining latent representations as the nature of inner product (i.e. the effect of multiplying small numbers) may cause *vanishing gradient* problems when we have a large number of sources of information (i.e.  $M$  is large). Furthermore, in some cases, the properties of predictive posterior given by ICK ensemble are dominated by the neural network as shown in Appendix K. It can sometimes be challenging to choose an appropriate NN architecture to make sure it does not interfere with other specified kernels.

**Broader Impacts** We believe our framework is extensively applicable to regression problems in many fields of study involving high-dimensional data and multiple sources of information with perceptible trends, such as remote sensing, spatial statistics, or clinical diagnosis. Also, we are not aware of any negative societal impacts of our work.

## 7. Conclusion

This paper presents a novel yet surprisingly simple Implicit Composite Kernel (ICK) framework to learn from *hybrid* data containing both high-dimensional information and low-dimensional information with prior knowledge. We first analytically show the resemblance between ICK and composite GPR models and then conduct experiments using both synthetic and real-world data. It appears that ICK outperforms various benchmark models in our experiments with lowest prediction errors and highest correlations even with very limited data. Overall, we show that our ICK framework

is exceptionally powerful when learning from *hybrid* data with prior knowledge incorporated, and we hope our work can inspire more future research on joint machine learning models, enhancing their performance, efficiency, flexibility, and generalization capability.

## References

- Al Imran, A., Amin, M. N., Rifat, M. R. I., and Mehreen, S. Deep neural network approach for predicting the productivity of garment employees. In *2019 6th International Conference on Control, Decision and Information Technologies (CoDIT)*, pp. 1402–1407. IEEE, 2019.
- Bishop, C. M. and Nasrabadi, N. M. *Pattern recognition and machine learning*, volume 4. Springer, 2006.
- Bottou, L., Curtis, F. E., and Nocedal, J. Optimization methods for large-scale machine learning. *Siam Review*, 60(2):223–311, 2018.
- Bouhlel, M. A. and Martins, J. R. Gradient-enhanced kriging for high-dimensional problems. *Engineering with Computers*, 35(1):157–173, 2019.
- Bouhlel, M. A., Bartoli, N., Otsmane, A., and Morlier, J. Improving kriging surrogates of high-dimensional design models by partial least squares dimension reduction. *Structural and Multidisciplinary Optimization*, 53(5):935–952, 2016.
- Bruinsma, W. P., Requeima, J., Foong, A. Y., Gordon, J., and Turner, R. E. The gaussian neural process. *arXiv preprint arXiv:2101.03606*, 2021.
- Choudhuri, N., Ghosal, S., and Roy, A. Nonparametric binary regression using a gaussian process prior. *Statistical Methodology*, 4(2):227–243, 2007.
- Datta, A., Banerjee, S., Finley, A. O., and Gelfand, A. E. Hierarchical nearest-neighbor gaussian process models for large geostatistical datasets. *Journal of the American Statistical Association*, 111(514):800–812, 2016.
- Dosovitskiy, A., Beyer, L., Kolesnikov, A., Weissenborn, D., Zhai, X., Unterthiner, T., Dehghani, M., Minderer, M., Heigold, G., Gelly, S., et al. An image is worth 16x16 words: Transformers for image recognition at scale. *arXiv preprint arXiv:2010.11929*, 2020.
- Drineas, P., Mahoney, M. W., and Cristianini, N. On the nyström method for approximating a gram matrix for improved kernel-based learning. *journal of machine learning research*, 6(12), 2005.
- Dua, D. and Graff, C. UCI machine learning repository, 2017. URL <http://archive.ics.uci.edu/ml>.
- Duvenaud, D. *Automatic model construction with Gaussian processes*. PhD thesis, University of Cambridge, 2014.
- Feydy, J. *Geometric data analysis, beyond convolutions*. PhD thesis, Université Paris-Saclay Gif-sur-Yvette, France, 2020.
- Gardner, J., Pleiss, G., Weinberger, K. Q., Bindel, D., and Wilson, A. G. Gpytorch: Blackbox matrix-matrix gaussian process inference with gpu acceleration. *Advances in neural information processing systems*, 31, 2018.
- Garnelo, M., Schwarz, J., Rosenbaum, D., Viola, F., Rezende, D. J., Eslami, S., and Teh, Y. W. Neural processes. *arXiv preprint arXiv:1807.01622*, 2018.
- Garriga-Alonso, A., Rasmussen, C. E., and Aitchison, L. Deep convolutional networks as shallow gaussian processes. *arXiv preprint arXiv:1808.05587*, 2018.
- Gelfand, A. E. and Schliep, E. M. Spatial statistics and gaussian processes: A beautiful marriage. *Spatial Statistics*, 18:86–104, 2016.
- Girolami, M. and Rogers, S. Variational bayesian multinomial probit regression with gaussian process priors. *Neural Computation*, 18(8):1790–1817, 2006.
- Goodfellow, I., Bengio, Y., and Courville, A. *Deep learning*. MIT press, 2016.
- He, B., Lakshminarayanan, B., and Teh, Y. W. Bayesian deep ensembles via the neural tangent kernel. *Advances in neural information processing systems*, 33:1010–1022, 2020.
- He, K., Chen, X., Xie, S., Li, Y., Dollár, P., and Girshick, R. Masked autoencoders are scalable vision learners. In *Proceedings of the IEEE/CVF Conference on Computer Vision and Pattern Recognition*, pp. 16000–16009, 2022.
- Hensman, J., Fusi, N., and Lawrence, N. D. Gaussian processes for big data. *arXiv preprint arXiv:1309.6835*, 2013.
- Jacot, A., Gabriel, F., and Hongler, C. Neural tangent kernel: Convergence and generalization in neural networks. *Advances in neural information processing systems*, 31, 2018.
- Jaderberg, M., Simonyan, K., Zisserman, A., et al. Spatial transformer networks. *Advances in neural information processing systems*, 28, 2015.
- Jiang, Z., Zheng, T., Bergin, M., and Carlson, D. Improving spatial variation of ground-level pm<sub>2.5</sub> prediction with contrastive learning from satellite imagery. *Science of Remote Sensing*, pp. 100052, 2022.

- Journel, A. G. and Huijbregts, C. J. *Mining geostatistics*. The Blackburn Press, 1976.
- Kim, H., Mnih, A., Schwarz, J., Garnelo, M., Eslami, A., Rosenbaum, D., Vinyals, O., and Teh, Y. W. Attentive neural processes. *arXiv preprint arXiv:1901.05761*, 2019.
- Kim, H.-M., Mallick, B. K., and Holmes, C. C. Analyzing nonstationary spatial data using piecewise gaussian processes. *Journal of the American Statistical Association*, 100(470):653–668, 2005.
- Kingma, D. P. and Ba, J. Adam: A method for stochastic optimization. *arXiv preprint arXiv:1412.6980*, 2014.
- Krige, D. G. A statistical approach to some basic mine valuation problems on the witwatersrand. *Journal of the Southern African Institute of Mining and Metallurgy*, 52(6):119–139, 1951.
- Lagaris, I. E., Likas, A., and Fotiadis, D. I. Artificial neural networks for solving ordinary and partial differential equations. *IEEE transactions on neural networks*, 9(5): 987–1000, 1998.
- LeCun, Y., Bengio, Y., and Hinton, G. Deep learning. *nature*, 521(7553):436–444, 2015.
- Lee, J., Bahri, Y., Novak, R., Schoenholz, S. S., Pennington, J., and Sohl-Dickstein, J. Deep neural networks as gaussian processes. *arXiv preprint arXiv:1711.00165*, 2017.
- Lee, J., Xiao, L., Schoenholz, S., Bahri, Y., Novak, R., Sohl-Dickstein, J., and Pennington, J. Wide neural networks of any depth evolve as linear models under gradient descent. *Advances in neural information processing systems*, 32, 2019.
- Maddison, C. J., Mnih, A., and Teh, Y. W. The concrete distribution: A continuous relaxation of discrete random variables. *arXiv preprint arXiv:1611.00712*, 2016.
- Marcus, G. Deep learning: A critical appraisal. *arXiv preprint arXiv:1801.00631*, 2018.
- Markou, S., Requeima, J., Bruinsma, W., and Turner, R. Efficient gaussian neural processes for regression. *arXiv preprint arXiv:2108.09676*, 2021.
- Matsubara, T., Oates, C. J., and Briol, F.-X. The ridgelet prior: A covariance function approach to prior specification for bayesian neural networks. *arXiv preprint arXiv:2010.08488*, 2020.
- Matthews, A. G. d. G., Hron, J., Turner, R. E., and Ghahramani, Z. Sample-then-optimize posterior sampling for bayesian linear models. In *NeurIPS Workshop on Advances in Approximate Bayesian Inference*, 2017.
- Matthews, A. G. d. G., Rowland, M., Hron, J., Turner, R. E., and Ghahramani, Z. Gaussian process behaviour in wide deep neural networks. *arXiv preprint arXiv:1804.11271*, 2018.
- McFee, B., Lanckriet, G., and Jebara, T. Learning multi-modal similarity. *Journal of machine learning research*, 12(2), 2011.
- Moseley, B., Markham, A., and Nissen-Meyer, T. Solving the wave equation with physics-informed deep learning. *arXiv preprint arXiv:2006.11894*, 2020.
- Neal, R. M. Priors for infinite networks. In *Bayesian Learning for Neural Networks*, pp. 29–53. Springer, 1996.
- Novak, R., Xiao, L., Hron, J., Lee, J., Alemi, A. A., Sohl-Dickstein, J., and Schoenholz, S. S. Neural tangents: Fast and easy infinite neural networks in python. In *International Conference on Learning Representations*, 2020. URL <https://github.com/google/neural-tangents>.
- Pearce, T., Tsuchida, R., Zaki, M., Brintrup, A., and Neely, A. Expressive priors in bayesian neural networks: Kernel combinations and periodic functions. In *Uncertainty in artificial intelligence*, pp. 134–144. PMLR, 2020.
- Petelin, D., Grancharova, A., and Kocijan, J. Evolving gaussian process models for prediction of ozone concentration in the air. *Simulation modelling practice and theory*, 33: 68–80, 2013.
- Rahimi, A. and Recht, B. Random features for large-scale kernel machines. *Advances in neural information processing systems*, 20, 2007.
- Rahimi, A. and Recht, B. Weighted sums of random kitchen sinks: Replacing minimization with randomization in learning. *Advances in neural information processing systems*, 21, 2008.
- Shi, T. and Horvath, S. Unsupervised learning with random forest predictors. *Journal of Computational and Graphical Statistics*, 15(1):118–138, 2006.
- Snelson, E. and Ghahramani, Z. Sparse gaussian processes using pseudo-inputs. *Advances in neural information processing systems*, 18, 2005.
- Van der Wilk, M., Rasmussen, C. E., and Hensman, J. Convolutional gaussian processes. *Advances in Neural Information Processing Systems*, 30, 2017.
- Vaswani, A., Shazeer, N., Parmar, N., Uszkoreit, J., Jones, L., Gomez, A. N., Kaiser, Ł., and Polosukhin, I. Attention is all you need. *Advances in neural information processing systems*, 30, 2017.

- Wang, H., He, H., and Katabi, D. Continuously indexed domain adaptation. *International Conference on Machine Learning*, 2020.
- Williams, C. and Seeger, M. Using the nyström method to speed up kernel machines. *Advances in neural information processing systems*, 13, 2000.
- Williams, C. K. and Barber, D. Bayesian classification with gaussian processes. *IEEE Transactions on pattern analysis and machine intelligence*, 20(12):1342–1351, 1998.
- Williams, C. K. and Rasmussen, C. E. *Gaussian processes for machine learning*, volume 2. MIT press Cambridge, MA, 2006.
- Wilson, A. and Adams, R. Gaussian process kernels for pattern discovery and extrapolation. In *International conference on machine learning*, pp. 1067–1075. PMLR, 2013.
- Wilson, A. G., Knowles, D. A., and Ghahramani, Z. Gaussian process regression networks. *arXiv preprint arXiv:1110.4411*, 2011.
- Wilson, A. G., Hu, Z., Salakhutdinov, R., and Xing, E. P. Deep kernel learning. In *Artificial intelligence and statistics*, pp. 370–378. PMLR, 2016.
- Yang, T., Li, Y.-F., Mahdavi, M., Jin, R., and Zhou, Z.-H. Nyström method vs random fourier features: A theoretical and empirical comparison. *Advances in neural information processing systems*, 25, 2012.
- Zhang, D., Wang, Y., Zhou, L., Yuan, H., Shen, D., Initiative, A. D. N., et al. Multimodal classification of alzheimer’s disease and mild cognitive impairment. *Neuroimage*, 55(3):856–867, 2011.
- Zheng, T., Bergin, M. H., Hu, S., Miller, J., and Carlson, D. E. Estimating ground-level pm<sub>2.5</sub> using micro-satellite images by a convolutional neural network and random forest approach. *Atmospheric Environment*, 230:117451, 2020.
- Zheng, T., Bergin, M., Wang, G., and Carlson, D. Local pm<sub>2.5</sub> hotspot detector at 300 m resolution: A random forest–convolutional neural network joint model jointly trained on satellite images and meteorology. *Remote Sensing*, 13(7):1356, 2021.
- Zhou, D., Kang, B., Jin, X., Yang, L., Lian, X., Jiang, Z., Hou, Q., and Feng, J. Deepvit: Towards deeper vision transformer. *arXiv preprint arXiv:2103.11886*, 2021.

## A. Further Discussion on Theorem 1

### A.1. A More Detailed Proof for Theorem 1

In this section, we provide a more detailed proof for Theorem 1. Again, suppose we have data  $\mathbf{X} = [\mathbf{x}_i]_{i=1}^N$  with information from 2 different sources  $\mathbf{x} = \{\mathbf{x}^{(1)}, \mathbf{x}^{(2)}\}$  where  $\mathbf{x}^{(1)} \in \mathbb{R}^{D_1}$  is high-dimensional and  $\mathbf{x}^{(2)} \in \mathbb{R}^{D_2}$  is low-dimensional with some known relationship with the targets  $\mathbf{Y} = [y_i]_{i=1}^N$ . With ICK formulation, we have  $\mathbf{z}^{(1)} = f_{\text{NN}}(\mathbf{x}^{(1)}) \in \mathbb{R}^p$  where  $f_{\text{NN}}$  is a NN-implied function with parameters  $\theta^{(1)}$  and  $\mathbf{z}^{(2)} = g(\mathbf{x}^{(2)}) \in \mathbb{R}^p$  where  $g$  is a kernel-to-latent-space mapping specified by a chosen kernel function  $K^{(2)}$  with parameters  $\theta^{(2)}$ . In Section 3.3, it is stated that the latent representation  $\mathbf{z}^{(1)}$  from  $f_{\text{NN}}$  will converge in distribution to a multi-output GP in the infinite width limit. In case when the NN has finite width,  $\mathbf{z}^{(1)}$  will *approximately* follows a GP with empirical NNGP kernel function  $\hat{K}^{\text{NNGP}}$

$$\mathbf{z}^{(1)} \sim \mathcal{GP}_{\text{approx}}(0, \hat{K}^{\text{NNGP}}). \quad (16)$$

Let  $\mathbf{Z}^{(1)} = [\mathbf{z}_i^{(1)}]_{i=1}^N$ . If Assumption 4.2 holds, then  $\mathbf{Z}^{(1)}$  can be approximately treated as a sample from a multivariate Gaussian as shown below

$$\mathbf{Z}^{(1)} \sim \mathcal{N}(\mathbf{0}, \hat{K}^{\text{NNGP}}), \quad (17)$$

where  $\mathbf{Z}^{(1)} \in \mathbb{R}^{N \times p}$  and  $\hat{K}^{\text{NNGP}} \in \mathbb{R}^{Np \times Np}$  is the corresponding kernel matrix

$$\hat{K}^{\text{NNGP}} = \begin{bmatrix} \hat{K}_1^{\text{NNGP}} & \mathbf{0} & \cdots & \mathbf{0} \\ \mathbf{0} & \hat{K}_2^{\text{NNGP}} & \cdots & \mathbf{0} \\ \vdots & \vdots & \ddots & \vdots \\ \mathbf{0} & \mathbf{0} & \cdots & \hat{K}_p^{\text{NNGP}} \end{bmatrix}, \quad (18)$$

and  $\hat{K}_k^{\text{NNGP}} = [\hat{K}_k^{\text{NNGP}}(\mathbf{x}_i^{(1)}, \mathbf{x}_j^{(1)})]_{i,j=1,\dots,N} \in \mathbb{R}^{N \times N}$  for all  $k = 1, 2, \dots, p$ . Also, since all entries in  $\mathbf{z}^{(1)}$  are from the same NN architecture with parameters drawn from the same distribution, as we increase the NN width, all  $\hat{K}_1^{\text{NNGP}}, \dots, \hat{K}_p^{\text{NNGP}}$  will converge to a deterministic limit. Therefore, in the finite-width case, it is reasonable to say that  $\hat{K}_1^{\text{NNGP}} \approx \dots \approx \hat{K}_p^{\text{NNGP}} \approx \hat{K}^{\text{NNGP}}$ . Based on the marginalization property of GPs (Williams & Rasmussen, 2006), any  $\mathbf{z}_i^{(1)} \in \mathbb{R}^p$  in  $\mathbf{Z}^{(1)}$  should *approximately* satisfy

$$\mathbf{z}_i^{(1)} \sim \mathcal{N}(\mathbf{0}, \hat{K}^{\text{NNGP}}(\mathbf{x}_i^{(1)}, \mathbf{x}_i^{(1)}) \mathbf{I}_p), \quad (19)$$

where  $\mathbf{I}_p$  is a  $p \times p$  identity matrix. In other words, each entry in  $\mathbf{z}_i^{(1)}$  has a univariate Gaussian distribution

$$z_{ik}^{(1)} \sim \mathcal{N}(0, \hat{K}^{\text{NNGP}}(\mathbf{x}_i^{(1)}, \mathbf{x}_i^{(1)})), k = 1, 2, \dots, p. \quad (20)$$

Let  $\alpha_{ik} = z_{ik}^{(2)} = g(\mathbf{x}_i^{(2)})_k$ , since the final output is  $\hat{y} = f_{\text{ICK}}(\mathbf{x}^{(1)}, \mathbf{x}^{(2)}) = \mathbf{z}^{(1)T} \mathbf{z}^{(2)}$ , for the  $i^{\text{th}}$  data point,  $\hat{y}_i$  can be viewed as a weighted sum of  $p$  independent Gaussian random variables under Assumption 4.2

$$\hat{y}_i \sim \sum_{k=1}^p \alpha_{ik} \mathcal{N}(0, \hat{K}^{\text{NNGP}}(\mathbf{x}_i^{(1)}, \mathbf{x}_i^{(1)})) = \sum_{k=1}^p \mathcal{N}(0, \alpha_{ik}^2 \hat{K}^{\text{NNGP}}(\mathbf{x}_i^{(1)}, \mathbf{x}_i^{(1)})) = \mathcal{N}\left(0, \hat{K}^{\text{NNGP}}(\mathbf{x}_i^{(1)}, \mathbf{x}_i^{(1)}) \sum_{k=1}^p \alpha_{ik}^2\right). \quad (21)$$

Therefore, the joint distribution of the final predictions of the whole training set  $\hat{\mathbf{Y}} = [\hat{y}_i]_{i=1}^N$  will be a multivariate Gaussian as given below

$$\hat{\mathbf{Y}} \sim \mathcal{N}\left(\mathbf{0}, \sum_{k=1}^p \begin{bmatrix} \alpha_{1k}^2 \hat{K}^{\text{NNGP}}(\mathbf{x}_1^{(1)}, \mathbf{x}_1^{(1)}) & \alpha_{1k} \alpha_{2k} \hat{K}^{\text{NNGP}}(\mathbf{x}_1^{(1)}, \mathbf{x}_2^{(1)}) & \cdots & \alpha_{1k} \alpha_{Nk} \hat{K}^{\text{NNGP}}(\mathbf{x}_1^{(1)}, \mathbf{x}_N^{(1)}) \\ \alpha_{2k} \alpha_{1k} \hat{K}^{\text{NNGP}}(\mathbf{x}_2^{(1)}, \mathbf{x}_1^{(1)}) & \alpha_{2k}^2 \hat{K}^{\text{NNGP}}(\mathbf{x}_2^{(1)}, \mathbf{x}_2^{(1)}) & \cdots & \alpha_{2k} \alpha_{Nk} \hat{K}^{\text{NNGP}}(\mathbf{x}_2^{(1)}, \mathbf{x}_N^{(1)}) \\ \vdots & \vdots & \ddots & \vdots \\ \alpha_{Nk} \alpha_{1k} \hat{K}^{\text{NNGP}}(\mathbf{x}_N^{(1)}, \mathbf{x}_1^{(1)}) & \alpha_{Nk} \alpha_{2k} \hat{K}^{\text{NNGP}}(\mathbf{x}_N^{(1)}, \mathbf{x}_2^{(1)}) & \cdots & \alpha_{Nk}^2 \hat{K}^{\text{NNGP}}(\mathbf{x}_N^{(1)}, \mathbf{x}_N^{(1)}) \end{bmatrix}\right), \quad (22)$$

which can be simplified as

$$\hat{\mathbf{Y}} \sim \mathcal{N}\left(\mathbf{0}, \sum_{k=1}^p \boldsymbol{\alpha}_k \boldsymbol{\alpha}_k^T * \hat{\mathbf{K}}^{\text{NNGP}}\right) = \mathcal{N}\left(\mathbf{0}, \boldsymbol{\alpha} \boldsymbol{\alpha}^T \odot \hat{\mathbf{K}}^{\text{NNGP}}\right), \quad (23)$$

where  $\boldsymbol{\alpha}_k = [\alpha_{ik}]_{i=1}^N \in \mathbb{R}^N$ ,  $\boldsymbol{\alpha} = [\alpha_{ik}]_{i=1, \dots, N, k=1, \dots, p} \in \mathbb{R}^{N \times p}$ ,  $\hat{\mathbf{K}}^{\text{NNGP}} = [\hat{K}^{\text{NNGP}}(\mathbf{x}_i^{(1)}, \mathbf{x}_j^{(1)})]_{i,j=1, \dots, N}$ , and " $\odot$ " represents elementwise multiplication. Therefore, if  $g$  includes the kernel-to-latent-space mapping  $K^{(2)}(\mathbf{x}_i^{(2)}, \mathbf{x}_j^{(2)}) \approx \mathbf{z}_i^{(2)T} \mathbf{z}_j^{(2)} = g(\mathbf{x}_i^{(2)})^T g(\mathbf{x}_j^{(2)})$ ,  $i, j = 1, \dots, N$  as shown in Equation 5, then  $\mathbf{K}^{(2)} = \boldsymbol{\alpha} \boldsymbol{\alpha}^T$  and we derive that

$$\hat{\mathbf{Y}} \sim \mathcal{N}\left(\mathbf{0}, \hat{\mathbf{K}}^{\text{NNGP}} \odot \mathbf{K}^{(2)}\right). \quad (24)$$

Since this derivation reasonably holds for any finite set of  $\mathbf{X}$  and  $\mathbf{Y}$ , we say the ICK framework is *approximately* equivalent to a GP with zero mean and a multiplicative kernel between the NNGP kernel matrix  $\hat{\mathbf{K}}^{\text{NNGP}}$  and the user-specified kernel matrix  $\mathbf{K}^{(2)}$ .

### A.2. A More Detailed Discussion on Assumption 4.2

As stated in Section 4.1 and the previous section, Theorem 4.1 relies heavily on Assumption 4.2 which assumes that all entries in  $z^{(1)}$  (the representation extracted by the neural network) are independent with each other. To show the validity of this assumption, we can explicitly write the  $k^{th}$  entry in  $z^{(1)}$  as follows:

$$z_k^{(1)}(\cdot) = b_k^{(1)} + \sum_{r=1}^{N_{z^{(1)}}} W_{kr}^{(1)} \phi \left( z_r'^{(1)}(\cdot) \right), \quad (25)$$

where  $W_{kr}^{(1)}$  and  $b_k^{(1)}$  are i.i.d. Gaussian weight and bias parameters and  $z_r'^{(1)}$  is the  $r^{th}$  entry in the previous layer. We see that  $z_k^{(1)}$  is a linear combination of i.i.d. Gaussian terms, and we can show that  $z_k^{(1)}(x_i)$  and  $z_l^{(1)}(x_j)$  are independent for two different inputs  $x_i$  and  $x_j$  and  $k \neq l$  by computing the covariance as shown below.

$$\begin{aligned} & \text{cov} \left( z_k^{(1)}(x_i), z_l^{(1)}(x_j) \right) \\ &= \mathbb{E} \left[ \left( b_k^{(1)} + \sum_{r=1}^{N_{z^{(1)}}} W_{kr}^{(1)} \phi \left( z_r'^{(1)}(x_i) \right) \right) \left( b_l^{(1)} + \sum_{s=1}^{N_{z^{(1)}}} W_{ls}^{(1)} \phi \left( z_s'^{(1)}(x_j) \right) \right) \right] \\ &= \mathbb{E} \left[ b_k^{(1)} b_l^{(1)} \right] + \mathbb{E} \left[ b_k^{(1)} \sum_{s=1}^{N_{z^{(1)}}} W_{ls}^{(1)} \phi \left( z_s'^{(1)}(x_j) \right) \right] + \mathbb{E} \left[ b_l^{(1)} \sum_{r=1}^{N_{z^{(1)}}} W_{kr}^{(1)} \phi \left( z_r'^{(1)}(x_i) \right) \right] \\ &+ \mathbb{E} \left[ \left( \sum_{r=1}^{N_{z^{(1)}}} W_{kr}^{(1)} \phi \left( z_r'^{(1)}(x_i) \right) \right) \left( \sum_{s=1}^{N_{z^{(1)}}} W_{ls}^{(1)} \phi \left( z_s'^{(1)}(x_j) \right) \right) \right] \end{aligned}$$

Since the weights and biases are all i.i.d. Gaussian with zero mean *a priori* and they are independent of the outputs from the previous layer, we have:

$$\begin{aligned} & \mathbb{E} \left[ b_k^{(1)} b_l^{(1)} \right] = \mathbb{E} \left[ b_k^{(1)} \right] \mathbb{E} \left[ b_l^{(1)} \right] = 0 \\ & \mathbb{E} \left[ b_k^{(1)} \sum_{s=1}^{N_{z^{(1)}}} W_{ls}^{(1)} \phi \left( z_s'^{(1)}(x_j) \right) \right] = \mathbb{E} \left[ b_k^{(1)} \right] \sum_{s=1}^{N_{z^{(1)}}} \mathbb{E} \left[ W_{ls}^{(1)} \phi \left( z_s'^{(1)}(x_j) \right) \right] = 0 \\ & \mathbb{E} \left[ b_l^{(1)} \sum_{r=1}^{N_{z^{(1)}}} W_{kr}^{(1)} \phi \left( z_r'^{(1)}(x_i) \right) \right] = \mathbb{E} \left[ b_l^{(1)} \right] \sum_{r=1}^{N_{z^{(1)}}} \mathbb{E} \left[ W_{kr}^{(1)} \phi \left( z_r'^{(1)}(x_i) \right) \right] = 0 \\ & \mathbb{E} \left[ \left( \sum_{r=1}^{N_{z^{(1)}}} W_{kr}^{(1)} \phi \left( z_r'^{(1)}(x_i) \right) \right) \left( \sum_{s=1}^{N_{z^{(1)}}} W_{ls}^{(1)} \phi \left( z_s'^{(1)}(x_j) \right) \right) \right] \\ &= \sum_{r=1}^{N_{z^{(1)}}} \sum_{s=1}^{N_{z^{(1)}}} \mathbb{E} \left[ W_{kr}^{(1)} W_{ls}^{(1)} \phi \left( z_r'^{(1)}(x_i) \right) \phi \left( z_s'^{(1)}(x_j) \right) \right] \\ &= \sum_{r=1}^{N_{z^{(1)}}} \sum_{s=1}^{N_{z^{(1)}}} \mathbb{E} \left[ W_{kr}^{(1)} \right] \mathbb{E} \left[ W_{ls}^{(1)} \right] \mathbb{E} \left[ \phi \left( z_r'^{(1)}(x_i) \right) \phi \left( z_s'^{(1)}(x_j) \right) \right] = 0. \end{aligned}$$

Therefore, we have  $\text{cov} \left( z_k^{(1)}(x_i), z_l^{(1)}(x_j) \right) = 0$ , meaning that  $z_{ik}^{(1)}$  and  $z_{jl}^{(1)}$  are uncorrelated with each other *a priori*, which shows the validity of Assumption 4.2. However, we do not claim the validity of this assumption *a posteriori*.

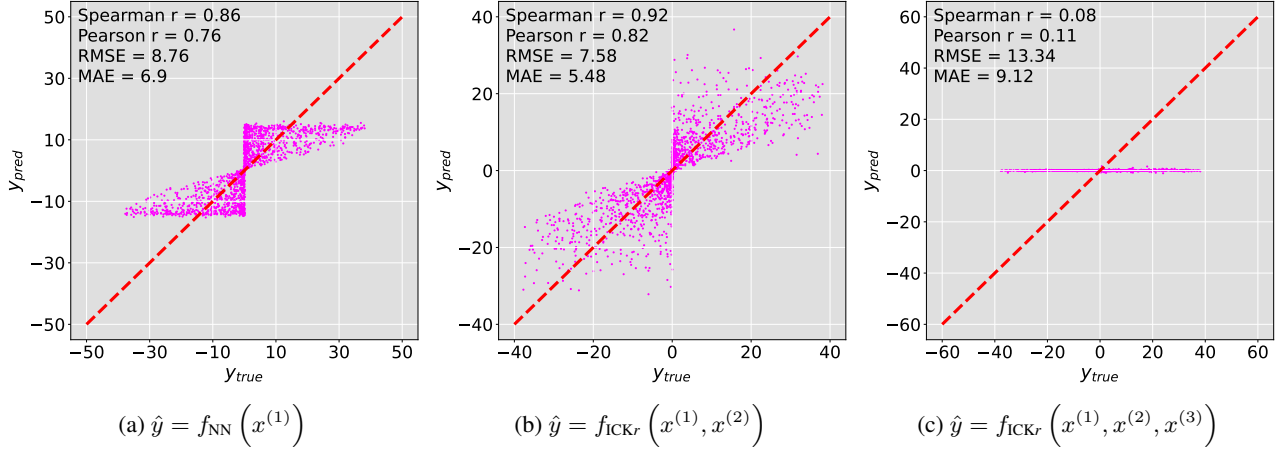


Figure B1. Scatter plots of the true values of  $y$  against the predicted values of  $y$  using our ICKr framework with (a) one source of information, (b) 2 sources of information, and (c) 3 sources of information. Note that here we use RFF for kernel-to-latent-space transformation.

## B. Random Fourier Features

### B.1. Methodology

Random Fourier Features (RFF) is another popular approximation method used for kernel learning (Rahimi & Recht, 2007). Unlike the Nyström method which approximates the entire kernel matrix, RFF directly approximates the kernel function  $K$  using some randomized feature mapping  $\phi: \mathbb{R}^{D_m} \rightarrow \mathbb{R}^{2d_m}$  such that  $K(x_i^{(m)}, x_j^{(m)}) \approx \phi(x_i^{(m)})^T \phi(x_j^{(m)})$ . To obtain the feature mapping  $\phi$ , based on Bochner’s theorem, we first compute the Fourier transform  $p$  of kernel  $K$

$$p(\omega) = \frac{1}{(2\pi)^{D_m}} \int_{-\infty}^{+\infty} e^{-j\omega^T \delta} K(\delta) d\delta, \quad (26)$$

where  $\delta = x_i^{(m)} - x_j^{(m)}$ . Then we draw  $d_m$  i.i.d. samples  $\omega_1, \omega_2, \dots, \omega_{d_m}$  from  $p(\omega)$  and construct the feature mapping  $\phi$  as follows

$$\phi(x^{(m)}) \equiv d_m^{-1/2} [\cos(\omega_1^T x^{(m)}), \dots, \cos(\omega_{d_m}^T x^{(m)}), \sin(\omega_1^T x^{(m)}), \dots, \sin(\omega_{d_m}^T x^{(m)})]. \quad (27)$$

Since  $\phi(x^{(m)}) \in \mathbb{R}^{2d_m}$ , we need to set  $d_m = p/2$  when using RFF as a kernel-to-latent-space transformation. In addition, since RFF involves sampling from a distribution, the kernel parameters are thus not directly differentiable and we need to apply a reparameterization trick (Maddison et al., 2016) to learn those parameters.

### B.2. Experimental Results

#### B.2.1. SYNTHETIC DATA

We use the same toy data set where each data point  $x = \{x^{(1)}, x^{(2)}, x^{(3)}\}$  contains 3 sources of information as described in Appendix F. Also, we use the same types of kernels as those in ICKy as discussed in Appendix F. The only difference here is that we use RFF instead of Nyström method to transform the kernel matrix into the latent space in ICKr framework.

The results are displayed in Figure B1. It can be observed that when we add in only the side information  $x^{(2)}$  along with the *exponential sine squared* kernel, both the correlation and the predictive performance are improved (though not as good as the results from ICKy as shown in Figure F1). However, after we further include  $x^{(3)}$  with the *RBF* kernel, we realize that the parameters of ICKr become very hard to optimize and it fails to make valid predictions and starts to guess randomly around zero.

#### B.2.2. REMOTE SENSING DATA

We also try ICKr on the *forecasting* task using the remote sensing data (see Section 5.2) and compare the results with those from ICKy. Each data point  $x = \{x, t\}$  contains a satellite image  $x$  as the high-dimensional information and its

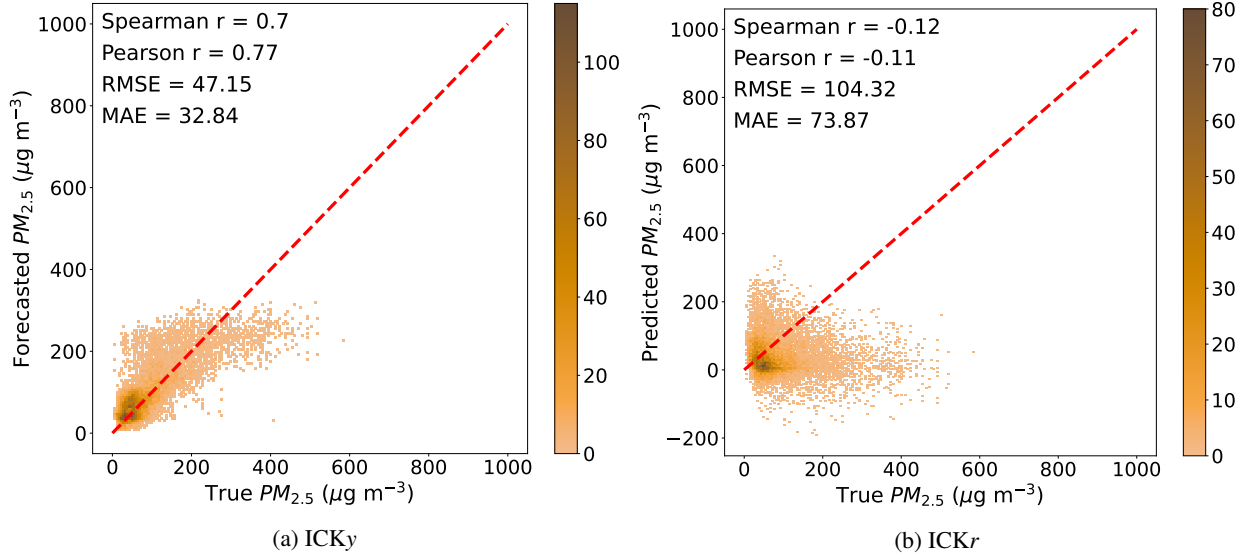


Figure B2. Density plots of the true  $PM_{2.5}$  concentrations against the forecasted  $PM_{2.5}$  concentrations for  $t \geq 500$  using our ICK framework with (a) ICKy and (b) ICKr

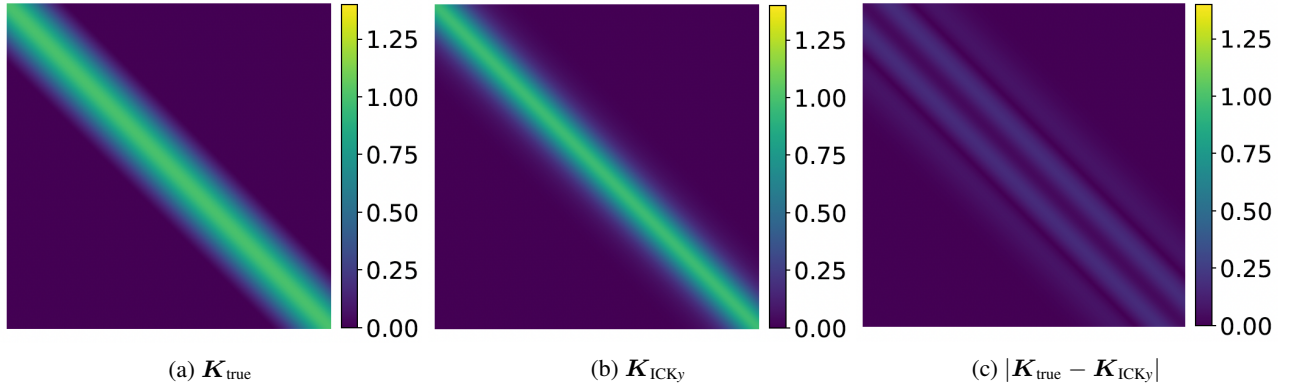


Figure C1. Visualization of (a) True matrix (b) estimated matrix by our ICKy framework, and (c) absolute difference between the true and estimated matrix for the spectral mixture kernel

corresponding timestamp  $t$  as the low-dimensional information. The satellite images are processed with a two-layer CNN and the timestamps are processed with an *exponential-sine-squared* kernel with a period of  $T = 365$  (days). As can be observed from Figure B2, ICKr yields much higher error compared to ICKy.

### C. Estimated Kernel Matrix and its Eigen-spectrum

We first examine whether ICKy can retrieve the spectral mixture kernel in the prediction task. After fitting the parameters of the spectral mixture kernel in ICKy, we compute the kernel matrix  $K_{\text{ICKy}}$  using these learned parameters and compare it with the true kernel matrix  $K_{\text{true}}$  by calculating the absolute difference between them as displayed in Figure C1. As can be observed,  $K_{\text{ICKy}}$  and  $K_{\text{true}}$  are similar and their absolute difference is relatively small, indicating that ICKy can approximately retrieve the spectral mixture kernel.

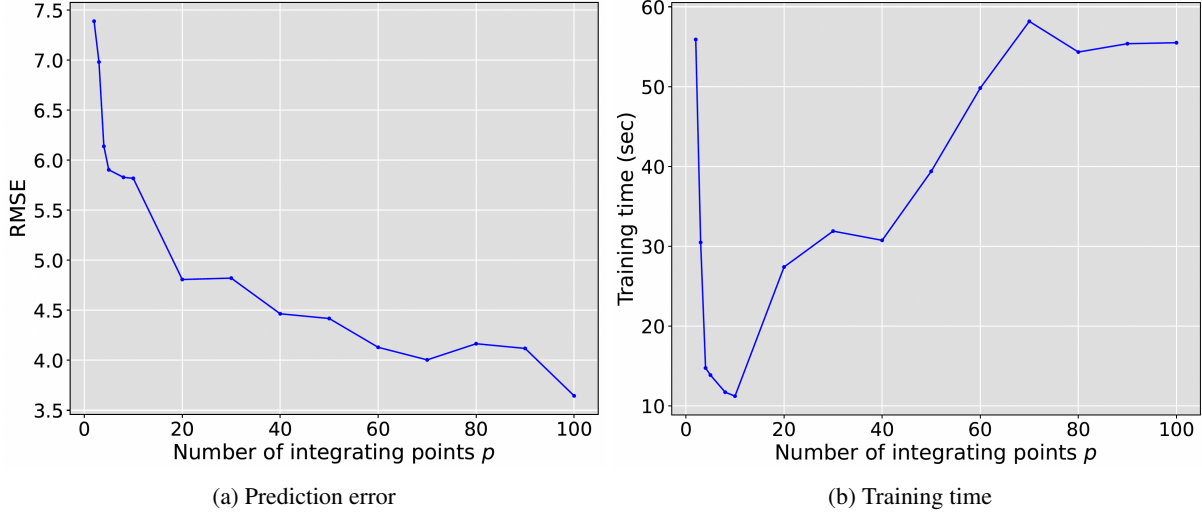


Figure D1. Plots of (a) prediction error and (b) training time of  $\hat{y} = f_{\text{ICK}_y}(x^{(1)}, x^{(2)}, x^{(3)})$  against the number of inducing points  $p$

Yang et al. (Yang et al., 2012) studied the fundamental difference between Nyström method and Random Fourier Features (RFF). They conclude that Nyström-method-based approaches can yield much better generalization error bound than RFF-based approaches if there exists a large gap in the eigen-spectrum of the kernel matrix. This phenomenon is mainly caused by how these two methods construct their basis functions. In particular, the basis functions used by RFF are sampled from a Gaussian distribution that is independent from the training examples, while the basis functions used by the Nyström method are sampled from the training samples so they are data-dependent. In our synthetic data experiments, we train our ICK framework using a batch size of 50. The eigenvalues of the kernel matrices computed from the first 4 batches of the synthetic data set are displayed in Figure C2. It can be observed that the first few eigenvalues of the kernel matrix are much larger than the remaining eigenvalues. Namely, there exists a large gap in the eigen-spectrum of the kernel matrix, which helps explain why ICK<sub>y</sub> has a much better performance than ICK<sub>r</sub>.

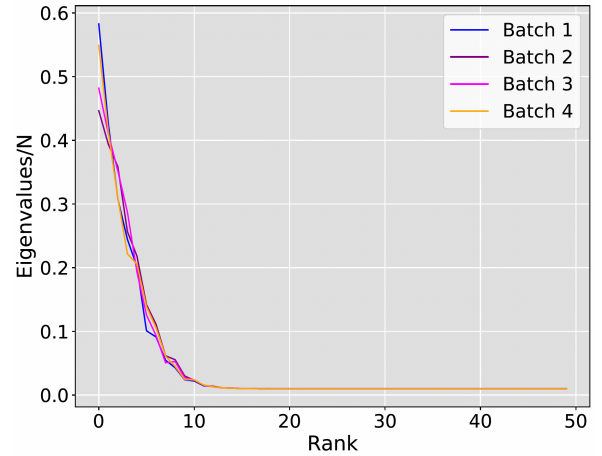


Figure C2. Eigenvalues of the kernel matrix computed from the first 4 batches of training data

## D. Number of Inducing Points

As discussed in Section 4.2.1, as we increase the number of inducing points  $p$ , we expect the approximation error between the true kernel matrix  $\mathbf{K}$  and the approximated kernel matrix  $\hat{\mathbf{K}}$  to decrease. Here, we empirically show how the value of  $p$  impacts our predictions. In Figure D1a, we plot the prediction error of  $\hat{y} = f_{\text{ICK}_y}(x^{(1)}, x^{(2)}, x^{(3)})$  against the number of inducing points using the synthetic data generated in Appendix F. As can be observed, the prediction error drops sharply as we raise  $p$  from a small value (e.g.  $p = 2$ ). When  $p$  is relatively large, increasing  $p$  yields smaller improvement on the predictions. Additionally, in Figure D1b, we plot the total training time against  $p$ . The total training time is dependent on how long a single iteration takes and the total number of epochs required. We note that once  $p > 80$  the training time is relatively flat, which is due to the fact that the total computation in the Cholesky is less than the computation in the neural network. Interestingly, it appears that when  $p$  is very small, ICK<sub>y</sub> takes longer to converge due to the need for many more epochs. As we increase  $p$ , the training time goes down and then goes up again due to the computational complexity, i.e.  $\mathcal{O}(p^3)$ , of the Cholesky decomposition. Based on these observations, we are not concerned about the computational complexity for reasonable values of  $p$ .

## E. Applying Sample-then-optimize Procedure to ICK

As elaborated in Section 4.3, a deep ensemble with proper initialization scheme will have a GP posterior interpretation in the infinite width limit when trained by a squared-error loss (He et al., 2020), which is an example of the "sample-then-optimize" procedure of Matthews et al. (Matthews et al., 2017) Algorithm 2 is an alternative to replace  $f_{\text{NN}}$  with such a deep ensemble  $F = \{f_{n_e}\}_{n_e=1}^{N_e}$  where the dimension of the final readout layer of each  $f_{n_e}$  is  $p$ . In this case, each baselearner  $f_{n_e}$  can be viewed as an i.i.d. sample from a multi-output GP in the infinite width limit. In the finite-width case, this relationship becomes approximate:

$$f_{n_e} \sim \mathcal{GP}_{\text{approx}}(0, K_F), \quad (28)$$

As stated by Lee et al. (Lee et al., 2019), if all the parameters in  $f_{n_e}$  are randomly drawn from a Gaussian distribution and are all fixed except the last layer, then after training  $F$  on a squared-error loss, we will have  $K_F \rightarrow K^{\text{NNGP}}$  where  $K^{\text{NNGP}}$  is the NNGP kernel. He et al. (He et al., 2020) also proposed to add a random and untrainable function  $\delta(\cdot)$  to the output of  $f_{n_e}$  so we have  $K_F \rightarrow K^{\text{NTK}}$  where  $K^{\text{NTK}}$  is the limiting NTK.

With ICK formulation, by following the proof given in Appendix A, we can derive that, for each baselearner in the ICK ensemble, the joint distribution of the final predictions of the whole training set  $\hat{Y}_{n_e}$  will again be a multivariate Gaussian as shown below if Assumption 4.2 holds *a posteriori*:

$$\hat{Y}_{n_e} \sim \mathcal{N}(\mathbf{0}, K_F \odot K^{(2)}), \quad (29)$$

where  $(K_F)_{ij} = K_F(\mathbf{x}_i^{(1)}, \mathbf{x}_j^{(1)})$ . Since Equation 29 holds for any finite input data set, we can conclude that each baselearner  $f_s$  in the ICK ensemble  $F_{\text{ICKy}} = \{f_s\}_{s=1}^{N_e}$  can be *approximately* viewed as an i.i.d. sample from a single-output GP

$$f_s \sim \mathcal{GP}_{\text{approx}}(0, K_F K^{(2)}) = \mathcal{GP}_{\text{approx}}(0, K^{\text{comp}}). \quad (30)$$

Building an ensemble  $F_{\text{ICKy}} = \{f_s\}_{s=1}^{N_e}$  is thus equivalent to performing a Monte Carlo approximation to a GP predictive posterior distribution whose mean and covariance matrix for a test data set  $\mathbf{X}^* = [\mathbf{x}_i^*]_{i=1}^{N^*}$  are

$$f_s(\mathbf{X}^* | \mathbf{X}) \sim \mathcal{N}(\boldsymbol{\mu}^*, \boldsymbol{\Sigma}^*), \quad (31)$$

$$\boldsymbol{\mu}^* = K_{X^*X}^{\text{comp}} (K_{XX}^{\text{comp}})^{-1} \mathbf{Y}, \quad (32)$$

$$\boldsymbol{\Sigma}^* = K_{X^*X^*}^{\text{comp}} - K_{X^*X}^{\text{comp}} (K_{XX}^{\text{comp}})^{-1} K_{XX^*}^{\text{comp}}, \quad (33)$$

where  $(K_{X^*X}^{\text{comp}})_{ij} = K^{\text{comp}}(\mathbf{x}_i^*, \mathbf{x}_j)$ ,  $(K_{XX}^{\text{comp}})_{ij} = K^{\text{comp}}(\mathbf{x}_i, \mathbf{x}_j)$ ,  $(K_{XX^*}^{\text{comp}})_{ij} = K^{\text{comp}}(\mathbf{x}_i^*, \mathbf{x}_j^*)$ , and  $K_{X^*X^*}^{\text{comp}} = (K_{XX^*}^{\text{comp}})^T$ . In other words, we can approximate the GP predictive posterior using the predictive mean and variance generated by Algorithm 2 as follows:

$$\hat{\boldsymbol{\mu}}^* = \frac{1}{N_e} \sum_{n=1}^{N_e} f_s(\mathbf{X}^* | \mathbf{X}) \approx \mathbb{E}[f_s(\mathbf{X}^* | \mathbf{X})] = \boldsymbol{\mu}^*, \quad (34)$$

$$\hat{\boldsymbol{\sigma}}^{*2} = \frac{1}{N_e} \sum_{n=1}^{N_e} [f_s(\mathbf{X}^* | \mathbf{X}) - \hat{\boldsymbol{\mu}}^*]^2 \approx \mathbb{V}[f_s(\mathbf{X}^* | \mathbf{X})] = \text{diag}(\boldsymbol{\Sigma}^*). \quad (35)$$

## F. ICK with More Than Two Kernels

Besides the visualization presented in Figure 1, we also show our ICK framework for processing data  $\mathbf{x} = \{x^{(1)}, x^{(2)}, \dots, x^{(M)}\}$  with  $M > 2$  sources of information in Figure F2. Here  $K^{(2)}, \dots, K^{(M)}$  represent different types of kernels with trainable parameters. The final prediction is calculated by a chained inner product of all extracted representations  $\hat{y} = \sum_{k=1}^p \prod_{m=1}^M z_k^{(m)}$ .

To confirm that ICKy can work with more than 2 kernels, we construct another synthetic data set containing 3000 data points in total. Each input  $\mathbf{x} = \{x^{(1)}, x^{(2)}, x^{(3)}\}$  has 3 sources of information. The output  $y$  is generated by  $y = x^{(3)} \tanh(2x^{(1)} \cos^2(\pi x^{(2)}/50)) + \epsilon$  where  $\epsilon$  is a Gaussian noise term. We process  $x^{(1)}$  with a small single-hidden-layer NN,  $x^{(2)}$  with an *exponential sine squared* kernel, and  $x^{(3)}$  with a *radial-basis function* (RBF) kernel. Figure F1 shows

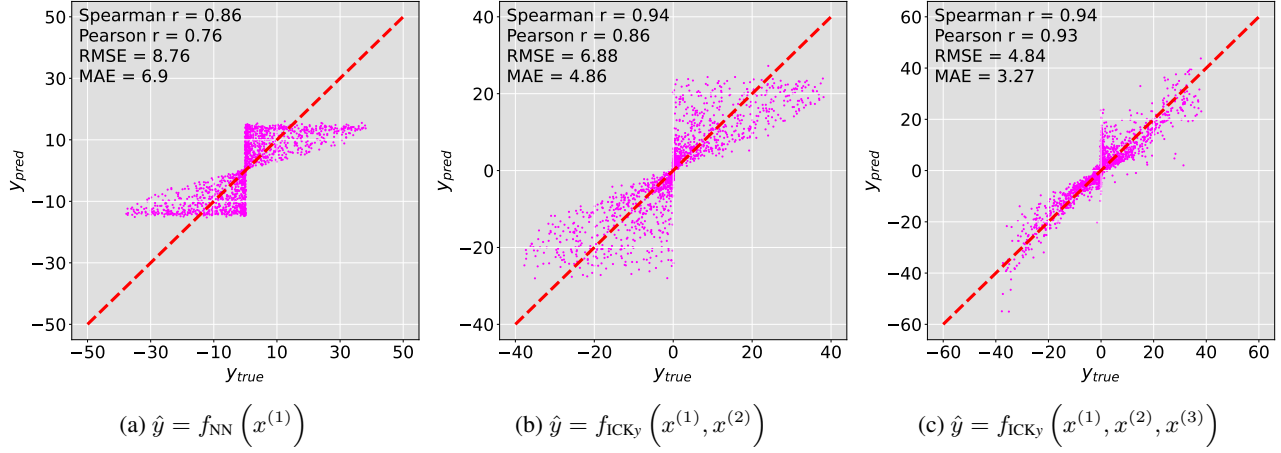


Figure F1. Scatter plots of the true values of  $y$  against the predicted values of  $y$  using our ICK<sub>y</sub> framework with (a) one source, (b) 2 sources, and (c) 3 sources of information

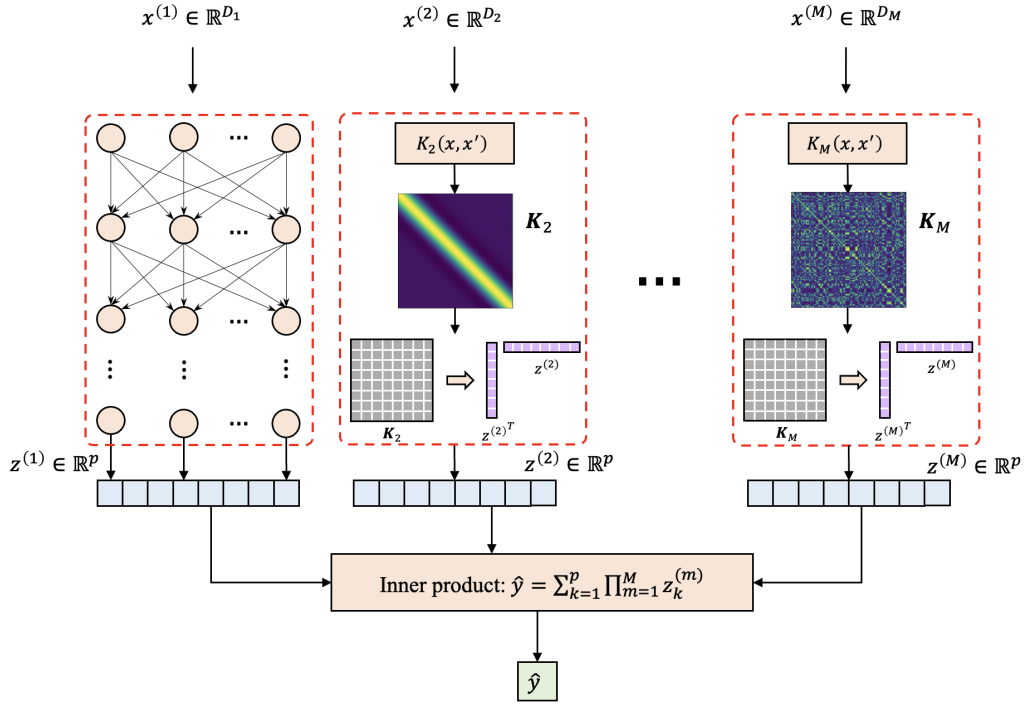


Figure F2. Given data containing  $M$  sources of information  $\mathbf{x} = \{x^{(1)}, x^{(2)}, \dots, x^{(M)}\}$ , we can process the data using our ICK framework where high-dimensional information (e.g.  $x^{(1)}$  in the figure) is processed using a neural network and low-dimensional information (e.g.  $x^{(2)}$  in the figure) is processed using a kernel function followed by Nyström or RFF transformation.

the prediction results as we progressively add more sources of information into our ICK<sub>y</sub> framework with corresponding kernel functions. It can be observed that ICK<sub>y</sub> yields both smallest error and highest correlation with information from all 3 different sources. Hence, ICK<sub>y</sub> works well with the  $M = 3$  case and the regression performance is improved as we add in more information related to the target.

Table 3. Model architecture and training details for remote sensing data experiment in Section 5.2

	Backbone architecture details	Output FC layers dimension	Optimizer
CNN-RF	# Conv blocks = 2, # Channels = 16, Kernel size = 3, Stride = 1	$1000 + d_{RT}$ , 512, 512, 1	Adam $\beta_1 = 0.9$ $\beta_2 = 0.999$
ViT-RF	# Transformer blocks = 2, # Attention heads = 8, Dropout ratio = 0.1	$1000 + d_{RT}$ , 512, 512, 1	Adam $\beta_1 = 0.9$ $\beta_2 = 0.999$
DeepViT-RF	# Transformer blocks = 2, # Attention heads = 8, Dropout ratio = 0.1	$1000 + d_{RT}$ , 512, 512, 1	Adam $\beta_1 = 0.9$ $\beta_2 = 0.999$
MAE-ViT-RF	# Transformer blocks = 2, # Attention heads = 8, Dropout ratio = 0.1, Masking ratio = 0.75	$1000 + d_{RT}$ , 512, 512, 1	Adam $\beta_1 = 0.9$ $\beta_2 = 0.999$
CNN-ICKy	# Conv blocks = 2, # Channels = 16, Kernel size = 3, Stride = 1	1000, 512, $p$	SGD momentum = 0.9
ViT-ICKy	# Transformer blocks = 2, # Attention heads = 8, Dropout ratio = 0.1	1000, 512, $p$	SGD momentum = 0.9
DeepViT-ICKy	# Transformer blocks = 2, # Attention heads = 8, Dropout ratio = 0.1	1000, 512, $p$	SGD momentum = 0.9

## G. Experimental Details

### G.1. Synthetic Data

We use the GPytorch package (Gardner et al., 2018) to generate the synthetic data. Before feeding  $x^{(1)}$  into MLP, we first map  $x^{(1)}$  into higher dimension using an unsupervised algorithm called Totally Random Trees Embedding (Shi & Horvath, 2006). All the MLP structures in this experiment (including those in MLP-RF and ICKy) contain one single fully connected (FC) layer of width 1000, which serves as a simple benchmark since a one-hidden-layer MLP can only capture linear relationship between the input and output. For model training, we optimize a Mean Squared Error (MSE) objective using Adam optimizer (Kingma & Ba, 2014) with a weight decay of 0.1.

### G.2. Remote Sensing Data

The model architecture and training details are listed in Table 3. Here  $p$  denotes the length of latent representations  $z$  as discussed in Section 4 and  $d_{RT}$  denotes the transformed dimension of timestamp  $t$  using the Random Trees Embedding as mentioned in Section G.1. Note that we use stochastic gradient descent (SGD) optimizer with a momentum of 0.9 for ICKy as we realize that SGD helps ICKy find a local minimum on the objective more efficiently. We use MSE objective for ICKy and all benchmark models in this experiment.

### G.3. Worker Productivity Data

The MLPs (including the MLP part in ICKy) in this experiment share the same structure as the one used in (Al Imran et al., 2019), which consist of 3 hidden layers of width 128, 32, and 32, respectively. For plain MLP, cyclic MLP, and ICKy, we use the mean absolute error (MAE) objective to put less weight on the outliers and thus enhance the model performance. For GNP and AGNP, we maximize a biased Monte Carlo estimate of the log-likelihood objective as discussed in (Markou et al., 2021). All these objectives are optimized by an Adam optimizer with  $\beta_1 = 0.9$  and  $\beta_2 = 0.999$ .

## H. Generation, Accessibility, and Restrictions of the Data

All experiments are conducted on a computer cluster equipped with a GeForce RTX 2080 Ti GPU. The synthetic data  $y \sim \mathcal{GP}(0, K_1 K_2)$  in Section 5.1 and  $y \sim \mathcal{GP}(0, K_1 + K_2)$  in Appendix J are generated using the GPyTorch package. The remote sensing data in Section 5.2 is downloaded using PlanetScope API whose content is protected by copyright and/or other intellectual property laws. To access the data on PlanetScope, the purchase of an end-user license is required. When this manuscript is accepted, we will provide the codes we used to acquire the data. The UCI machine learning repository data we use in Section 5.3 has an open access license, meaning that the data is freely available online.

## I. Adapting ICK for Classification

While regression tasks are the primary motivation for this paper, there are many ways to adapt GPR for classification tasks. For example, a binary classification model can be created by using a sigmoid (Williams & Barber, 1998) or probit link (Choudhuri et al., 2007) on the output of the GP. Succinctly, given a function  $f(\mathbf{x}) \sim \mathcal{GP}(0, K(\mathbf{x}, \mathbf{x}'))$ , the binary outcome probability is given as  $p(y = 1|f(\mathbf{x})) = \sigma(f(\mathbf{x}))$ . Likewise, a multiple classification model can be constructed by using a multi-output GP (or multiple GPs) and putting the outputs through a softmax function (Williams & Barber, 1998) or multinomial probit link (Girolami & Rogers, 2006). This strategy can be summarized by calculating  $C$  different functions  $f_c(\mathbf{x}) \sim \mathcal{GP}(0, K(\mathbf{x}, \mathbf{x}'))$  for  $c = 1, \dots, C$ , where  $C$  is the number of classes, and then calculating the class probabilities through a link function,  $p(y|\mathbf{x}) = \text{softmax}([f_1(\mathbf{x}), f_2(\mathbf{x}), \dots, f_C(\mathbf{x})])$ .

This same logic can be used to construct a multiple classification model from ICKy. Succinctly, let  $r_c = f_{\text{NN},c}(\mathbf{x}^{(1)}) \odot \mathbf{z}_c^{(2)}$ , where  $f_{\text{NN},c}$  denotes a neural network specific to the  $c^{\text{th}}$  class and  $\mathbf{z}_c^{(2)}$  represents the Nyström approximation specific to the kernel for the  $c^{\text{th}}$  class. We note that often in a multi-output case the kernel parameters are shared, and so  $\mathbf{z}_c^{(2)}$  would be an identical vector for each class. Then, the output probabilities for a data sample as  $p(y|\mathbf{x}) = \text{softmax}([r_1, \dots, r_C])$ . This framework is learned with a cross-entropy loss.

To provide *proof-of-concept* of this multiple classification strategy, we implemented this model on a version of Rotating MNIST. In this task, a dataset was created by rotating each image in the dataset by a uniform random value  $\phi \in [0, 2\pi)$ , thus creating a dataset with 60,000 images each with an associated rotation covariate  $\phi$ . We implemented the above multiple classification model with a periodic kernel over the rotation angle. This strategy yielded an accuracy of 92.3% on the validation data. This is lower than methods such as spatial transformers (Jaderberg et al., 2015) that report accuracy greater than 99%. However, those models explicitly use the fact that the information is simply rotated, whereas ICK is modeling a smooth transformation in the prediction function as a function of angle. This ICK classification model is much closer in concept to the way Rotating MNIST is used to evaluate unsupervised domain adaptation. While the evaluation strategy is different than our random validation set, the state-of-the-art accuracy on unsupervised domain adaption is 87.1% (Wang et al., 2020). Due to the lack of complete and fair comparisons, we are not claiming that ICKy is state-of-the-art for classification, but ICKy’s classification model does seem reasonable and viable based upon this result.

## J. Additional Results on Synthetic Data

To demonstrate the superior performance of ICKy more clearly, we also test plain MLP, MLP-RF, and ICKy on the prediction task in Section 5.1 using different number of training samples. As displayed in Figure J1a, ICKy yields the smallest error among all the 3 frameworks even with very limited data.

While ICK is theoretically designed to simulate posterior sampling from GPs with multiplicative kernels, to show its flexibility, we also evaluate how well it could simulate additive kernels. We conduct experiments using another synthetic data set generated by an additive kernel  $y \sim \mathcal{GP}(0, K_1 + K_2)$  with the same training settings. As shown in Figure J2, ICKy again outperforms plain MLP and MLP-RF. Moreover, we test plain MLP, MLP-RF, and ICKy on this task using different number of training samples. As displayed in Figure J1b, ICKy yields the smallest error among all the 3 frameworks. Also, the performance gap between ICKy and the other 2 benchmark models shrink as we feed in more training data. Therefore, we conclude ICKy is robust enough to simulate posterior sampling from GPs with both additive and multiplicative kernels.

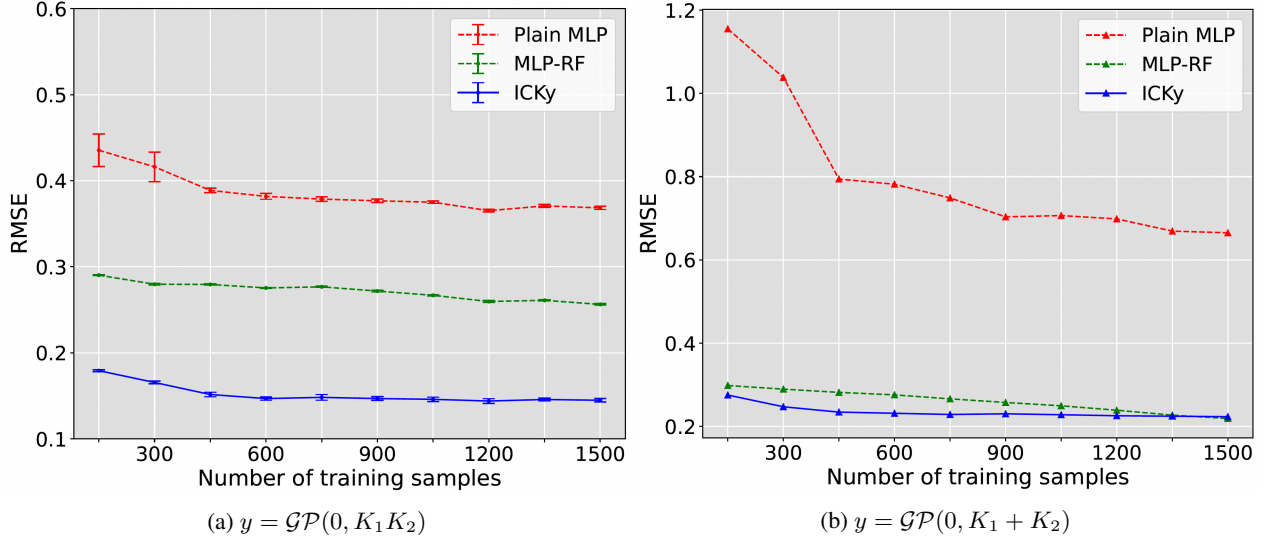


Figure J1. Prediction error of plain MLP, MLP-RF, and ICKy with different amount of training data generated by (a)  $y = \mathcal{GP}(0, K_1 K_2)$  and (b)  $y = \mathcal{GP}(0, K_1 + K_2)$

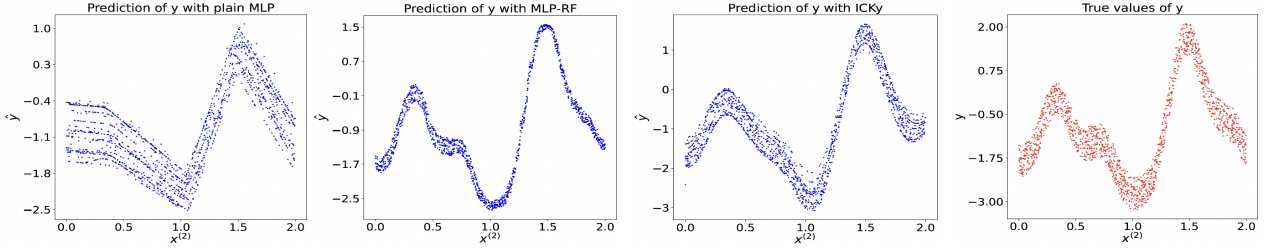


Figure J2. Prediction of  $y \sim \mathcal{GP}(0, K_1 + K_2)$ , where  $x^{(1)}$  is input to a linear kernel  $K_1$  and  $x^{(2)}$  is input to a spectral mixture kernel  $K_2$ . We plot  $x^{(2)}$  against the predicted  $y$ . We show results from a plain MLP (left), MLP-RF (middle left), and ICKy framework (middle right), and we compare to the true values of  $y$  (right).

## K. Time Series Visualization for Remote Sensing Experiment

To explore the problem of posterior uncertainty calibration for ViT variants of ICKy (i.e. extremely large MSLL as shown in Table 1), we visualize the results as time series by first grouping the predictions by the timestamp  $t$ , taking the *minimum* of the predictive variance, and plotting them along with the corresponding true values and the predictive mean as shown in Figure K1. The shaded region represents the confidence interval  $[\mu - 2\sigma, \mu + 2\sigma]$  where  $\mu$  and  $\sigma$  are the predictive mean and standard deviation of  $\text{PM}_{2.5}$ , respectively. We realize that CNN-ICKy ensemble tends to yield much higher variance than DeepViT-ICKy ensemble when the predictive mean deviates from the true values. A plausible explanation is that the DeepViT structure contains much more parameters than the CNN structure (21.80M vs 1.92M) used in our remote sensing experiment, which makes DeepViT-ICKy overparameterized (The DeepViT architecture is set to be consistent with the CNN architecture as shown in Table 3). To alleviate this problem, we try reducing the number of transformer blocks in ViT and DeepViT and we do observe a significant drop in MSLL.

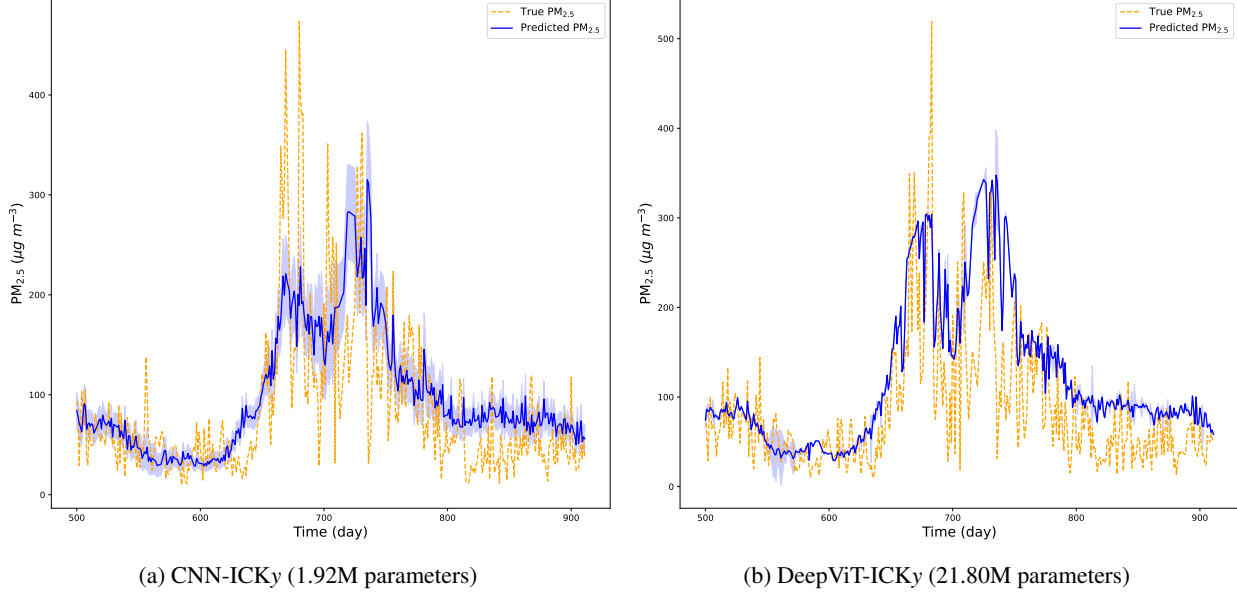


Figure K1. Time series visualization of predictive mean and uncertainty of  $PM_{2.5}$  in Section 5.2 (remote sensing experiment) for (a) CNN-ICKy and (b) DeepViT-ICKy

## L. Distance Between ICK Ensemble Posterior and its NNGP Counterpart

Besides Figure 2 in Section 4.3, we estimate the Wasserstein-1 distance between the predictive posterior of ICKy ensemble and its analytic NNGP counterpart using the de-biased Sinkhorn divergence (Feydy, 2020). As displayed in Figure L1, the Wasserstein-1 distance shows a decreasing trend as we increase the number of estimators  $N_e$  in the ICKy ensemble (except at  $N_e = 50$  where there might be some noise or perturbations in the sampling process from the posterior). This serves as a more convincing evidence, verifying the predictive posterior of ICKy ensemble will converge to its analytic NNGP counterpart. However, since we are using finite-width NN for each baselearner in the ICKy ensemble, there will be a gap between these two distributions and the Wasserstein-1 distance is not guaranteed to converge to zero.

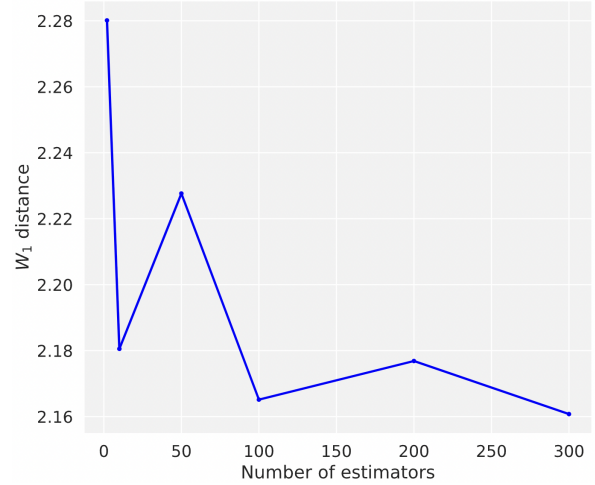


Figure L1. Wasserstein-1 distance between the predictive posterior of ICKy ensemble and its analytic NNGP counterpart